JGR Solid Earth

RESEARCH ARTICLE
10.1029/2021JB022365

Key Points:

- An anisotropic eikonal equation is derived to model first-arrival traveltimes in azimuthally anisotropic media
- Novel ray-free adjoint-state traveltime tomography and earthquake location methods are developed for azimuthally anisotropic media
- *P*-wave traveltime data reveal structural and stress-induced anisotropy in and off the San Andreas Fault zone, respectively

Supporting Information:

Supporting Information may be found in the online version of this article.

Correspondence to:

P. Tong,
tongping@ntu.edu.sg

Citation:

Tong, P. (2021). Adjoint-state traveltime tomography for azimuthally anisotropic media and insight into the crustal structure of central California near Parkfield. *Journal of Geophysical Research: Solid Earth*, *126*, e2021JB022365. https://doi.org/10.1029/2021JB022365

Received 10 MAY 2021
Accepted 10 SEP 2021

Adjoint-State Traveltime Tomography for Azimuthally Anisotropic Media and Insight Into the Crustal Structure of Central California Near Parkfield

Ping Tong[1,2,3]

[1]Division of Mathematical Sciences, School of Physical and Mathematical Sciences, Nanyang Technological University, Singapore, Singapore, [2]Asian School of the Environment, Nanyang Technological University, Singapore, Singapore, [3]Earth Observatory of Singapore, Nanyang Technological University, Singapore, Singapore

Abstract Seismic anisotropy provides crucial information on the stress state and geodynamic processes inside the Earth. We develop a novel adjoint-state traveltime tomography method using *P*-wave traveltime data to simultaneously determine velocity heterogeneity and azimuthal anisotropy of the subsurface. First, an anisotropic eikonal equation is derived to model first-arrival traveltimes in azimuthally anisotropic media. Traveltime tomography is then formulated as an optimization problem constrained by the anisotropic eikonal equation, which is subsequently solved by the adjoint-state method. Ray tracing is not required. Its high accuracy is achieved by solving the anisotropic eikonal equation and the associated adjoint equation with efficient numerical solvers. In addition, an eikonal equation-based earthquake location method for azimuthally anisotropic media is developed to solve the coupled hypocenter-velocity problem. The tomography and earthquake location methods are applied to central California near Parkfield to test their performance in practice. A total of 1,068,850 first *P*-wave traveltimes clearly maps the velocity heterogeneity and azimuthal anisotropy in the upper and middle crust. The average *P*-wave velocity model shows a striking velocity contrast across the San Andreas Fault (SAF). In the upper crust, we find structural anisotropy in the SAF zone and stress-induced anisotropy off the SAF zone. In the middle crust, the fast *P*-wave velocity directions are generally fault-parallel due to the decreased effect of the maximum horizontal compressive stress. In all, the real-data application suggests that the new adjoint-state traveltime tomography method can be reliably used to investigate anisotropic seismic structures.

Plain Language Summary This study is a sophisticated extension of the adjoint-state traveltime tomography method for isotropic media discussed in Tong (2021), https://doi.org/10.1029/2021JB021818. An anisotropic eikonal equation is derived to model first-arrival traveltimes in azimuthally anisotropic media. Following that, the adjoint-state traveltime tomography method and eikonal equation-based earthquake location method are developed for azimuthally anisotropic media. Neither ray tracing nor waveform modeling is required. The validity of the new methods is verified in central California near Parkfield, revealing structural anisotropy in the San Andreas Fault zone and stress-induced anisotropy off the fault zone.

1. Introduction

Seismic anisotropy describes the directional dependence of elastic properties measured at the same place. As widely observed in the crust, the upper mantle, the transition zone, the D" layer, and the inner core (Long & Becker, 2010), seismic anisotropy is a key indicator for the past and present deformation processes in the Earth's interior. The sources for seismic anisotropy vary in different regions. Stress-induced anisotropy caused by local/regional stress field and structure-induced anisotropy due to the presence of faults, sedimentation structures and mineral alignment are the two main types of seismic anisotropy observed in the upper crust (e.g., Boness & Zoback, 2006; Li & Peng, 2017). Seismic anisotropies in the lower crust, upper mantle and mantle transition zone are generally attributed to strain-induced lattice-preferred orientation (LPO) of materials, such as schists, olivine and wadsleyite, that occurs during tectonic and flow deformation (e.g., Kawazoe et al., 2013; Long & Silver, 2008; Porter et al., 2011). In addition to its wide existence, seismic anisotropy has the same level of effect as seismic heterogeneity on traveltime observations (Zhao et al., 2016). Ignoring seismic anisotropy in seismic data analysis may result in biased, inaccurate or even wrong interpretations of the subsurface structures and dynamic processes.

Body waves, surface waves, and ambient noise data all contain information contributed by seismic anisotropy. Accordingly, a plenty of tools have been developed to study seismic anisotropy in different regions of the Earth's interior by exploring different types of seismic data. Techniques using body waves include shear wave splitting, receiver function analysis, *Pn* anisotropy tomography, *P*-wave anisotropy tomography, and others (e.g., Bostock, 2003; Eberhart-Phillips & Henderson, 2004; Hearn, 1996; Silver & Chan, 1991). Shear wave splitting, which measures the fast polarization direction ϕ and the traveltime difference Δt between the fast and slow arrivals on either local or teleseismic shear waves, is a frequently used tool for seismic anisotropy investigation in the crust and mantle (Long, 2013; Savage, 1999). Although the technique is simple in theory, computationally inexpensive and possesses a good resolving ability in lateral directions, shear wave splitting has poor resolution in the vertical direction, especially when seismic anisotropy is resolved by core phases such as SKS and SKKS (Fouch & Rondenay, 2006; Long, 2013). Anisotropic receiver function analysis usually extracts seismic anisotropy information from teleseismic P-to- S conversions (e.g., Bar et al., 2019; Kong et al., 2018). It has extensive depth resolution at the wavelength scale of the P-to- S phase (Fouch & Rondenay, 2006), which is much higher than that of the shear wave splitting. However, anisotropic receiver function analysis always has difficulty in uniquely determining the multiple parameters describing an anisotropic medium from under-represented data (Fouch & Rondenay, 2006; Long, 2013). *P*-wave anisotropy tomography is capable of revealing 3-D variations of seismic anisotropy, requiring that the area of interest is fully illuminated by criss-crossing rays to balance the trade-off between seismic heterogeneity and anisotropy (Z. Huang et al., 2015; Long, 2013; Zhao et al., 2016). Pn waves place constraints on azimuthal anisotropy of the uppermost mantle (e.g., Basu & Powell, 2019; Hearn, 1996). The differential times of SS precursors provide constraints on seismic anisotropy of the mantle transition zone (Q. Huang et al., 2019). Notably, during the past decade, adjoint tomography based on numerically solving 3-D anisotropic elastic/viscoelastic wave equation has emerged as a new promising tool to construct anisotropic velocity models, which inverts body waves and surface waves sequentially or simultaneously or directly inverts the full waveform contents (e.g., Fichtner & Villasenor, 2015; Tromp et al., 2005; K. Wang et al., 2020; Zhu et al., 2015).

Azimuthal anisotropy and radial anisotropy are the two basic forms of anisotropy that have been extensively investigated by previous studies. Due to space limitations, the present work is focused on *P*-wave azimuthal anisotropy, but *P*-wave radial anisotropy will be discussed in a separate study. *P*-wave azimuthal anisotropy tomography is a proven powerful tool for studying seismic anisotropy of the crust and upper mantle (Zhao et al., 2016). Even though the recent wave equation-based adjoint tomography method can determine *P*-wave azimuthal anisotropy by choosing a proper elastic wave equation to simulate the propagation of seismic waves in azimuthally anisotropic media, due to its high computational cost and using mainly relatively stable low-frequency data, further efforts are required to make it a routine technique for imaging high-resolution seismic anisotropic structures. On the other hand, the ray-based *P*-wave azimuthal anisotropy tomography methods have been widely used to investigate seismic anisotropy inside the Earth in the past two decades or so (e.g., Eberhart-Phillips & Henderson, 2004; Liu & Tong, 2021; Tong et al., 2021; Wang & Zhao, 2008; Zhao et al., 2016). As is known, ray tracing is essential for ray-based seismic tomography methods. But conventional ray-tracing methods including the shooting method and bending method may fail to converge to the true path even in mildly heterogeneous media (Rawlinson et al., 2008). Furthermore, due to the increasing complexity of ray tracing in anisotropic media (Wang, 2014; Gou et al., 2018), it is a common practice to use seismic ray paths computed in isotropic media to approximate the corresponding ones in weakly anisotropic media (Tong et al., 2021). Obviously, this kind of approximation affects the accuracy of the computed traveltimes and the accuracy of the derivatives of the objective function with respect to anisotropic model parameters, and consequently distorts the final tomographic results to some extent.

In this study, we develop an alternative and robust seismic azimuthal anisotropy tomography method requiring no ray tracing. Technically, the new method is an extension of the previous adjoint-state traveltime tomography method for isotropic media (Tong, 2021). Initially, we derive an eikonal equation specifically for azimuthally anisotropic media. Then the optimization problem of seismic traveltime tomography is solved by the efficient adjoint-state method. Following that, the optimal azimuthally anisotropic velocity model is obtained by using the step-size-controlled gradient descent method in an iterative manner (Tong, 2021). In addition, a novel earthquake location method for azimuthally anisotropic media is developed to precisely locate earthquake hypocenters. The performance of the adjoint-state seismic azimuthal anisotropy tomography method and the earthquake location method is tested in the region of central California near

Parkfield, one of the most seismologically active areas in the world. Finally, the details of the upper crustal anisotropy revealed by the new tomography method together with its implications of crustal dynamics and earthquake occurrence are thoroughly discussed.

2. Adjoint-State Traveltime Tomography for Azimuthally Anisotropic Media

The adjoint-state traveltime tomography method for azimuthally anisotropic media is derived in this section. Particularly, the eikonal equation for azimuthally anisotropic media, the Fréchet derivatives of the traveltime objective function with respect to model parameters, the multiple-grid model parameterization, and the numerical methods are discussed in detail.

2.1. Eikonal Equation for Azimuthally Anisotropic Media

We consider the elliptical anisotropic eikonal equation with a point-source condition,

$$\begin{cases} \sqrt{\left[\nabla T(\mathbf{x})\right]^t M(\mathbf{x})\nabla T(\mathbf{x})} = 1, & \mathbf{x} \in \Omega \backslash \{\mathbf{x}_s\}, \\ T(\mathbf{x}_s) = 0, \end{cases} \tag{1}$$

where Ω can be viewed as the Earth volume, $T(\mathbf{x})$ is the traveltime field of a wave emanating from the source $\mathbf{x}_s$, the superscript t represents the transpose operation on the column vector $\nabla T(\mathbf{x})$, and $M(\mathbf{x})$ is a symmetric positive definite matrix describing material anisotropy (Luo & Qian, 2012). The anisotropic eikonal Equation 1 has been widely used in optics, mechanics, computer vision, geosciences, medical imaging, and many others (e.g., Luo & Qian, 2012; Qian et al., 2007). In this study, we show that it can be used to model seismic azimuthal anisotropy. We denote the three mutually orthogonal unit eigenvectors of $M(\mathbf{x})$ by $\mathbf{p}(\mathbf{x})$, $\mathbf{q}(\mathbf{x})$ and $\mathbf{r}(\mathbf{x})$. Physically, the eigenvalues indicate the squared velocities along the corresponding eigenvector directions. To be consistent with later discussion, the eigenvalues are denoted by $c_f^2(\mathbf{x})$, $c_s^2(\mathbf{x})$, and $c_z^2(\mathbf{x})$. Using basic matrix algebra, we have

$$M(\mathbf{x}) = c_f^2(\mathbf{x})\mathbf{p}(\mathbf{x}) \otimes \mathbf{p}(\mathbf{x}) + c_s^2(\mathbf{x})\mathbf{q}(\mathbf{x}) \otimes \mathbf{q}(\mathbf{x}) + c_z^2(\mathbf{x})\mathbf{r}(\mathbf{x}) \otimes \mathbf{r}(\mathbf{x}), \tag{2}$$

where the symbol $\otimes$ represents the outer product operation.

We turn to consider the propagation of a particular seismic wave (*P*, SV, or SH-wave but *P*-wave in the present study) in an azimuthally anisotropic medium with mirror symmetry (Figure 1). Both the fast velocity direction and the slow velocity direction are in the horizontal plane. Assume that the anti-clockwise angle of the fast-velocity direction with respect to the x-axis or the east is ϕ ($\phi + \pi$) and that the angle of the slow-velocity direction with respect to the x-axis or the east is $\phi + \frac{1}{2}\pi$ ($\phi + \frac{3}{2}\pi$). The fast velocity direction, the slow velocity direction and the vertical direction can be mathematically expressed by $\mathbf{p}(\mathbf{x}) = (\cos\phi(\mathbf{x}),\sin\phi(\mathbf{x}),0)^t$, $\mathbf{q}(\mathbf{x}) = (-\sin\phi(\mathbf{x}),\cos\phi(\mathbf{x}),0)^t$, and $\mathbf{r}(\mathbf{x}) = (0,0,1)^t$, which are mutually orthogonal. We further assume that the wave speeds in the fast-velocity direction, the slow-velocity direction, and the vertical direction are $c_f(\mathbf{x})$, $c_s(\mathbf{x})$ and $c_z(\mathbf{x})$, respectively. Without loss of generality, $c_f(\mathbf{x}) \geq c_s(\mathbf{x})$ is always assumed. Based on Equation 2, the anisotropic matrix $M(\mathbf{x})$ for the azimuthally anisotropic medium renders,

$$M(\mathbf{x}) = \begin{bmatrix} \frac{c_f^2(\mathbf{x}) + c_s^2(\mathbf{x})}{2} + \frac{c_f^2(\mathbf{x}) - c_s^2(\mathbf{x})}{2}\cos 2\phi(\mathbf{x}) & \frac{c_f^2(\mathbf{x}) - c_s^2(\mathbf{x})}{2}\sin 2\phi(\mathbf{x}) & 0 \\ \frac{c_f^2(\mathbf{x}) - c_s^2(\mathbf{x})}{2}\sin 2\phi(\mathbf{x}) & \frac{c_f^2(\mathbf{x}) + c_s^2(\mathbf{x})}{2} - \frac{c_f^2(\mathbf{x}) - c_s^2(\mathbf{x})}{2}\cos 2\phi(\mathbf{x}) & 0 \\ 0 & 0 & c_z^2(\mathbf{x}) \end{bmatrix}. \tag{3}$$

For the convenience of discussion, we define three functions $s(\mathbf{x})$, $\epsilon(\mathbf{x})$ and $\zeta(\mathbf{x})$:

$$s(\mathbf{x}) = \sqrt{\frac{2}{c_f^2(\mathbf{x}) + c_s^2(\mathbf{x})}}, \quad \epsilon(\mathbf{x}) = \frac{1}{2}\frac{c_f^2(\mathbf{x}) - c_s^2(\mathbf{x})}{c_f^2(\mathbf{x}) + c_s^2(\mathbf{x})}, \quad \zeta(\mathbf{x}) = \frac{c_z^2(\mathbf{x})}{c_f^2(\mathbf{x}) + c_s^2(\mathbf{x})} - \frac{1}{2}, \tag{4}$$

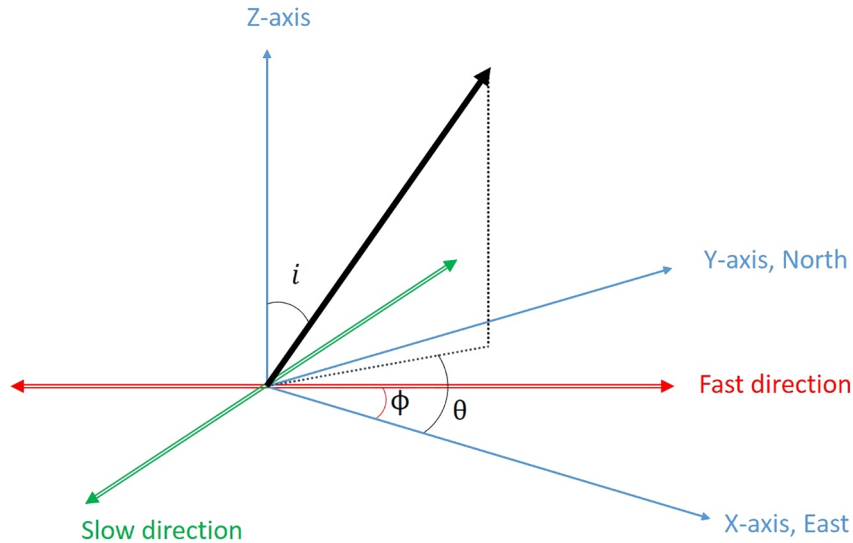

Figure 1. The local coordinates for an azimuthally anisotropic medium. The red and green double headed arrows denote the horizontal fast and slow directions, respectively. The black arrow shows the direction of wave propagation. i is the incident angle to the vertical z-axis. ϕ and θ measure the azimuthal angles of the fast velocity direction and the raypath to the x-axis or east, respectively. The y-axis points to the north.

and two additional functions $\xi(\mathbf{x})$ and $\eta(\mathbf{x})$:

$$\xi(\mathbf{x}) = \epsilon(\mathbf{x})\cos 2\phi(\mathbf{x}), \qquad \eta(\mathbf{x}) = \epsilon(\mathbf{x})\sin 2\phi(\mathbf{x}). \tag{5}$$

Then, the anisotropic matrix (3) can be simplified,

$$\begin{aligned} M(\mathbf{x}) &= \frac{1}{s^2(\mathbf{x})}\begin{bmatrix} 1+2\epsilon(\mathbf{x})\cos 2\phi(\mathbf{x}) & 2\epsilon(\mathbf{x})\sin 2\phi(\mathbf{x}) & 0 \\ 2\epsilon(\mathbf{x})\sin 2\phi(\mathbf{x}) & 1-2\epsilon(\mathbf{x})\cos 2\phi(\mathbf{x}) & 0 \\ 0 & 0 & 1+2\zeta(\mathbf{x}) \end{bmatrix} \\ &= \frac{1}{s^2(\mathbf{x})}\begin{bmatrix} 1+2\xi(\mathbf{x}) & 2\eta(\mathbf{x}) & 0 \\ 2\eta(\mathbf{x}) & 1-2\xi(\mathbf{x}) & 0 \\ 0 & 0 & 1+2\zeta(\mathbf{x}) \end{bmatrix}. \end{aligned} \tag{6}$$

Following that, the eikonal Equation 1 for azimuthally anisotropic media can be written as

$$\left[\nabla T(\mathbf{x})\right]^t \begin{bmatrix} 1+2\xi(\mathbf{x}) & 2\eta(\mathbf{x}) & 0 \\ 2\eta(\mathbf{x}) & 1-2\xi(\mathbf{x}) & 0 \\ 0 & 0 & 1+2\zeta(\mathbf{x}) \end{bmatrix} \nabla T(\mathbf{x}) = s^2(\mathbf{x}). \tag{7}$$

We examine the wave speed in any arbitrary direction to show that the traveltime field described by the anisotropic eikonal Equation 7 is equal to the traveltime field computed along explicit rays under the assumption of weak anisotropy. In a locally homogeneous anisotropic medium, given any two points $\mathbf{x} = (x, y, z)$ and $\mathbf{x} + \Delta\mathbf{x} = (x + \Delta r\cos\theta\sin i, y + \Delta r\sin\theta\sin i, z + \Delta r\cos i)$, where θ is the azimuth angle to the x-axis and i is the incident angle to the vertical axis (Figure 1). According to Luo and Qian (2012), the traveltime increment $\Delta T(\mathbf{x})$ between them is

$$\Delta T(\mathbf{x}) = s(\mathbf{x})\Delta r\sqrt{\frac{(1+2\zeta)\left[1-2\epsilon\cos 2(\phi-\theta)\right]\sin^2 i + (1-4\epsilon^2)\cos^2 i}{(1+2\zeta)(1-4\epsilon^2)}}. \tag{8}$$

Thus, in the direction $(\cos\theta\sin i, \sin\theta\sin i, \cos i)$ the slowness is

$$S(\mathbf{x},\theta,i) = s(\mathbf{x})\sqrt{\frac{1-2\epsilon\cos 2(\phi-\theta)}{1-4\epsilon^2}\sin^2 i + \frac{1}{1+2\zeta}\cos^2 i}. \tag{9}$$

Under the assumption of weak anisotropy, that is, $|\epsilon(\mathbf{x})| \ll 1$ and $|\zeta(\mathbf{x})| \ll 1$, the directional slowness can be approximated by the first-degree Taylor polynomial of the right hand side of Equation 9 as

$$S(\mathbf{x},\theta,i) \approx s(\mathbf{x})\left[1-\epsilon\cos 2(\theta-\phi)\sin^2 i-\zeta\cos^2 i\right]. \tag{10}$$

In previous ray-based azimuthal anisotropy tomography studies (e.g., Eberhart-Phillips & Henderson, 2004; Z. Wang et al., 2008; Zhao et al., 2016), the *P*-wave slowness in the horizontal plane is usually approximated by $S(\mathbf{x},\theta,90°) = s(\mathbf{x})\left[1-\epsilon\cos 2(\theta-\phi)\right]$, which is the same as the approximation (10). Nevertheless, it is challenging to precisely trace ray paths in anisotropic media, while the traveltime field $T(\mathbf{x})$ can be accurately computed by solving the anisotropic eikonal Equation 7 with an efficient numerical algorithm (Bouteiller et al., 2019; Eaton, 1993; Qian et al., 2007).

The anisotropic eikonal Equation 7 contains four model parameters $s(\mathbf{x})$, $\xi(\mathbf{x})$, $\eta(\mathbf{x})$, and $\zeta(\mathbf{x})$. We ought to resolve all of them via seismic tomographic inversions. However, multiple parameters inversion still faces many challenges. If possible, the number of model parameters involved in seismic inversions should be maintained at the minimum level. Hence, we make the following three assumptions so that the anisotropic eikonal Equation 7 can be described by three model parameters: (a) $\zeta(\mathbf{x}) = 0$, that is, $c_z(\mathbf{x}) = 1/s(\mathbf{x})$; (b) $\zeta(\mathbf{x}) = \epsilon(\mathbf{x})$, that is, $c_z(\mathbf{x}) = c_f(\mathbf{x})$; (c) $\zeta(\mathbf{x}) = -\epsilon(\mathbf{x})$, that is, $c_z(\mathbf{x}) = c_s(\mathbf{x})$. In a uniform form, $\zeta(\mathbf{x}) = \gamma\epsilon(\mathbf{x}) = \gamma\sqrt{\xi^2(\mathbf{x})+\eta^2(\mathbf{x})}$, where $\gamma = 0, 1, -1$. For each assumption, only $\epsilon(\mathbf{x})$ characterizes the magnitude of azimuthal anisotropy. Similar assumptions have been made in previous seismic azimuthal anisotropy studies (e.g., Eberhart-Phillips & Henderson, 2004; Zhao et al., 2016). Hereinafter, we use the following eikonal equation to describe the traveltime field of the first arrival in azimuthally anisotropic media

$$\left[\nabla T(\mathbf{x})\right]^t \begin{bmatrix} 1+2\xi(\mathbf{x}) & 2\eta(\mathbf{x}) & 0 \\ 2\eta(\mathbf{x}) & 1-2\xi(\mathbf{x}) & 0 \\ 0 & 0 & 1+2\gamma\sqrt{\xi^2(\mathbf{x})+\eta^2(\mathbf{x})} \end{bmatrix} \nabla T(\mathbf{x}) = s^2(\mathbf{x}). \tag{11}$$

We continue to discuss how to choose γ among its three possible values. As reported by Eberhart-Phillips and Henderson (2004), the results obtained with different choices of γ are virtually the same and the differences in the amplitude of recovered seismic anisotropy are less than one per cent. For brevity, the investigation of the minor differences caused by choosing different γ values is reserved for future studies. In all the synthetic and real data examples to be presented later, we assume that the vertical velocity is equal to the azimuthal average in the horizontal plane by setting $\gamma = 0$.

2.2. Fréchet Derivatives

First *P*-wave arrivals from N earthquakes $\mathbf{x}_{s,n}$ $(n = 1,2,\ldots,N)$ are recorded by M seismic stations $\mathbf{x}_{r,m}$ $(m = 1,2,\ldots,M)$. An optimal azimuthally anisotropic velocity model $\left(s(\mathbf{x}),\xi(\mathbf{x}),\eta(\mathbf{x})\right)$ can be found by minimizing the objective function below

$$\chi\left(s(\mathbf{x}),\xi(\mathbf{x}),\eta(\mathbf{x})\right) = \sum_{n=1}^{N}\sum_{m=1}^{M}\frac{\omega_{n,m}}{2}\left[T_n(\mathbf{x}_{r,m}) - T_n^o(\mathbf{x}_{r,m})\right]^2, \tag{12}$$

where $T_n(\mathbf{x}_{r,m})$ and $T_n^o(\mathbf{x}_{r,m})$ are the calculated and observed traveltimes, respectively; $\omega_{n,m}$ reflects the existence or quality of the seismic arrival corresponding to the n-th earthquake and m-th seismic station. The first-order derivatives $\partial\chi/\partial s$, $\partial\chi/\partial\xi$ and $\partial\chi/\partial\eta$ are usually required to find the optimum value of the objective function $\chi\left(s(\mathbf{x}),\xi(\mathbf{x}),\eta(\mathbf{x})\right)$,which can be derived by using the adjoint-state method (Appendix A). The first-order derivatives can be specifically expressed in a form involving sensitivity kernels

$$\delta\chi\left(s(\mathbf{x}),\xi(\mathbf{x}),\eta(\mathbf{x})\right) = \int_\Omega K_s(\mathbf{x})\frac{\delta s(\mathbf{x})}{s(\mathbf{x})}d\mathbf{x} + \int_\Omega K_\xi(\mathbf{x})\delta\xi(\mathbf{x})d\mathbf{x} + \int_\Omega K_\eta(\mathbf{x})\delta\eta(\mathbf{x})d\mathbf{x}. \tag{13}$$

The respective sensitivity kernels with respect to the slowness $s(\mathbf{x})$ and two anisotropic parameters $\xi(\mathbf{x})$ and $\eta(\mathbf{x})$ are

$$K_s(\mathbf{x}) = \sum_{n=1}^{N} P_n(\mathbf{x})s^2(\mathbf{x}), \tag{14}$$

$$K_\xi(\mathbf{x}) = \sum_{n=1}^{N}\left[\nabla T_n(\mathbf{x})\right]^t \begin{bmatrix} -1 & 0 & 0 \\ 0 & 1 & 0 \\ 0 & 0 & -\dfrac{\gamma}{\sqrt{\xi^2(\mathbf{x})+\eta^2(\mathbf{x})}} \end{bmatrix} \nabla T_n(\mathbf{x}) P_n(\mathbf{x}), \tag{15}$$

$$K_\eta(\mathbf{x}) = \sum_{n=1}^{N}\left[\nabla T_n(\mathbf{x})\right]^t \begin{bmatrix} 0 & -1 & 0 \\ -1 & 0 & 0 \\ 0 & 0 & -\dfrac{\gamma}{\sqrt{\xi^2(\mathbf{x})+\eta^2(\mathbf{x})}} \end{bmatrix} \nabla T_n(\mathbf{x}) P_n(\mathbf{x}), \tag{16}$$

where $P_n(\mathbf{x})$ is the adjoint field satisfying $P_n(\mathbf{x}) = 0$ on $\partial\Omega$ and

$$\begin{aligned} &\nabla\cdot\left\{P_n(\mathbf{x})\left[-\nabla T_n(\mathbf{x})\right]^t \begin{bmatrix} 1+2\xi(\mathbf{x}) & 2\eta(\mathbf{x}) & 0 \\ 2\eta(\mathbf{x}) & 1-2\xi(\mathbf{x}) & 0 \\ 0 & 0 & 1+2\gamma\sqrt{\xi^2(\mathbf{x})+\eta^2(\mathbf{x})} \end{bmatrix}\right\} \\ &= \sum_{m=1}^{M}\omega_{n,m}\left[T_n(\mathbf{x}) - T_n^o(\mathbf{x}_{r,m})\right]\delta(\mathbf{x}-\mathbf{x}_{r,m}), \quad \mathbf{x}\in\Omega\backslash\{\mathbf{x}_s\}. \end{aligned} \tag{17}$$

2.3. Model Parameterization

We choose the multiple-grid model parameterization (Tong et al., 2019) to discretize the model perturbations $\delta s(\mathbf{x})/s(\mathbf{x})$, $\delta\xi(\mathbf{x})$ and $\delta\eta(\mathbf{x})$. A multiple-grid usually consists of multiple regular component grids placed in a staggered way (Tong, 2021). The grid nodes of the h-th component grid are denoted by (X_i^h, Y_j^h, Z_k^h) $(1\le i\le N_x^h, 1\le j\le N_y^h, 1\le k\le N_z^h, 1\le h\le H)$. Every grid node (X_i^h, Y_j^h, Z_k^h) is associated with one basis function $B_l^h(\mathbf{x}) = B_l^h(x,y,z)$ $(l = (k-1)N_x^hN_y^h + (j-1)N_x^h + i)$, which is defined by

$$B_l^h(x,y,z) = w_i^h(x)w_j^h(y)w_k^h(z), \tag{18}$$

where

$$w_i^h(x) = \begin{cases} \dfrac{x - X_{i-1}^h}{X_i^h - X_{i-1}^h}, & \text{if } X_1^h \le X_{i-1}^h \le x \le X_i^h, \\ \dfrac{X_{i+1}^h - x}{X_{i+1}^h - X_i^h}, & \text{if } X_i^h \le x \le X_{i+1}^h \le X_{N_x}^h, \\ 0, & \text{otherwise,} \end{cases} \tag{19}$$

and similarly for $w_j^h(y)$ and $w_k^h(z)$. On each component grid, the relative slowness perturbation $\delta s(\mathbf{x})/s(\mathbf{x})$ can be expanded as a linear combination of the basis functions $B_l^h(\mathbf{x})(h = 1,\ldots,H; l = 1,\ldots,L_h; L_h = N_x^hN_y^hN_z^h)$

$$\frac{\delta s(\mathbf{x})}{s(\mathbf{x})} = \sum_{l=1}^{L_h}\delta C_l^h B_l^h(\mathbf{x}). \tag{20}$$

Considering that every component grid can be selected indiscriminately to define the relative slowness perturbation, we use the average to approximate $\delta s(\mathbf{x})/s(\mathbf{x})$, that is,

$$\frac{\delta s(\mathbf{x})}{s(\mathbf{x})} = \frac{1}{H}\sum_{h=1}^{H}\sum_{l=1}^{L_h}\delta C_l^h B_l^h(\mathbf{x}). \tag{21}$$

Similarly, the perturbations $\delta\xi(\mathbf{x})$ and $\delta\eta(\mathbf{x})$ can be approximated by

$$\delta\xi(\mathbf{x}) = \frac{1}{H_\xi}\sum_{h=1}^{H_\xi}\sum_{l=1}^{L_{h,\xi}}\delta C_{l,\xi}^h B_{l,\xi}^h(\mathbf{x}) \tag{22}$$

and

$$\delta\eta(\mathbf{x}) = \frac{1}{H_\eta}\sum_{h=1}^{H_\eta}\sum_{l=1}^{L_{h,\eta}}\delta C_{l,\eta}^{h} B_{l,\eta}^{h}(\mathbf{x}). \tag{23}$$

Plugging Equations 21–23 in Equation 13, we have

$$\frac{\partial\chi\left(s(\mathbf{x}),\xi(\mathbf{x}),\eta(\mathbf{x})\right)}{\partial C_l^h} = \frac{1}{H}\int_\Omega K_s(\mathbf{x}) B_l^h(\mathbf{x}) d\mathbf{x}, \tag{24}$$

$$\frac{\partial\chi\left(s(\mathbf{x}),\xi(\mathbf{x}),\eta(\mathbf{x})\right)}{\partial C_{l,\xi}^h} = \frac{1}{H_\xi}\int_\Omega K_\xi(\mathbf{x}) B_{l,\xi}^h(\mathbf{x}) d\mathbf{x}, \tag{25}$$

$$\frac{\partial\chi\left(s(\mathbf{x}),\xi(\mathbf{x}),\eta(\mathbf{x})\right)}{\partial C_{l,\eta}^h} = \frac{1}{H_\eta}\int_\Omega K_\eta(\mathbf{x}) B_{l,\eta}^h(\mathbf{x}) d\mathbf{x}. \tag{26}$$

After the implementation of model parameterization, the optimization problem 12 searching for an optimal azimuthally anisotropic velocity model ($s(\mathbf{x})$, $\xi(\mathbf{x})$, $\eta(\mathbf{x})$) in infinite-dimensional function spaces is reduced to a minimization problem in a finite-dimensional vector space. Once the first-order partial derivatives (24–26) are computed, we can find an optimal vector $(C_1^1,\ldots,C_{L_1}^1,C_1^2,\ldots,C_{L_H}^H,C_{1,\xi}^1,\ldots,C_{L_1,\xi}^1,C_{1,\xi}^2,\ldots,C_{L_H,\xi}^H,C_{1,\eta}^1,\ldots,C_{L_1,\eta}^1,C_{1,\eta}^2,\ldots,C_{L_H,\eta}^H)$ by using the method of gradient descent, conjugate gradient method or some others (e.g., Fletcher & Reeves, 1964; Tromp et al., 2005; Virieux & Operto, 2009). In this study, a step-size-controlled gradient descent method which has an effect of damping optimization is utilized to find the optimal solution in an iterative manner (Tong, 2021).

2.4. Numerical Methods

Both the anisotropic eikonal Equation 11 and the adjoint Equation 17 are numerically solved on a dense forward grid. As constrained by the resolving ability of seismic traveltime data, the forward grid is much denser than every component grid of the multiple-grid (the inversion grid). To perform numerical computations, we discretize the forward traveltime field $T_n(\mathbf{x})$, the adjoint field $P_n(\mathbf{x})$, the model parameters $s(\mathbf{x})$, $\xi(\mathbf{x})$, $\eta(\mathbf{x})$, the sensitivity kernels $K_s(\mathbf{x})$, $K_\xi(\mathbf{x})$, $K_\eta(\mathbf{x})$, and the model perturbations $\Delta s(\mathbf{x})/s(\mathbf{x})$, $\Delta\xi(\mathbf{x})$, $\Delta\eta(\mathbf{x})$ all on the forward grid. Particularly, in every iteration, we determine the coefficients $(\Delta C_1^1,\ldots,\Delta C_{L_H}^H,\Delta C_{1,\xi}^1,\ldots,\Delta C_{L_H,\xi}^H,\Delta C_{1,\eta}^1,\ldots,\Delta C_{L_H,\eta}^H)$ on the inversion grid first to obtain the functions (21–23) in the continuous Earth volume Ω, then we discretize the model perturbations $\Delta s(\mathbf{x})/s(\mathbf{x})$, $\Delta\xi(\mathbf{x})$, $\Delta\eta(\mathbf{x})$ on the forward grid and update the models on the forward grid.

The fast sweeping method for a class of static convex Hamilton-Jacobi equations (Luo & Qian, 2012; Qian et al., 2007) is applied to solve the anisotropic eikonal Equation 11, which is an accurate, efficient, and causality enforced numerical algorithm that converges in a finite number of iterations (Qian et al., 2007). Different from Luo and Qian (2012), the anisotropic eikonal equation is neither additively nor multiplicatively factorized. But the source singularity is mitigated by adopting the local homogenization strategy: The analytical solution, computed with the model parameters at the source location, is directly assigned to the forward grid nodes that are within three grid intervals from the source in any coordinate directions. The adjoint Equation 17 is solved by a different fast sweeping method designed specifically for the transport equation in a form of $(aP_n)_x + (bP_n)_y + (cP_n)_z = 0$ (Leung & Qian, 2006), where a, b and c are given functions of (x,y,z). In our numerical implementation, an extra value of $\omega_{n,m}\left[T_n(\mathbf{x}) - T_n^o(\mathbf{x}_{r,m})\right]/(\Delta x\Delta y\Delta z)$ is added to the computed $P_n(\mathbf{x}_{r,m})$ at every receiver location $\mathbf{x}_{r,m}$. If $\mathbf{x}_{r,m}$ does not coincide with any grid node, trilinear interpolation applies. Here Δx, Δy and Δz are the intervals of the forward grid. The fast sweeping method for the adjoint Equation 17 also has a good property of convergence (Leung & Qian, 2006).

2.5. Synthetic Example

We use a synthetic example to verify the adjoint-state traveltime tomography method for azimuthally anisotropic media. First P-wave arrivals of 100 earthquakes recorded by 60 seismic stations are inverted to reconstruct the average slowness $s(\mathbf{x})$ and two anisotropic parameters $\xi(\mathbf{x})$ and $\eta(\mathbf{x})$ (Figures 2a–2c). The earthquakes and seismic stations are located in the same plane and their lateral coordinates are random numbers between 0 and 100 (Figures 2b and 2c). The starting model is homogeneous and isotropic, which

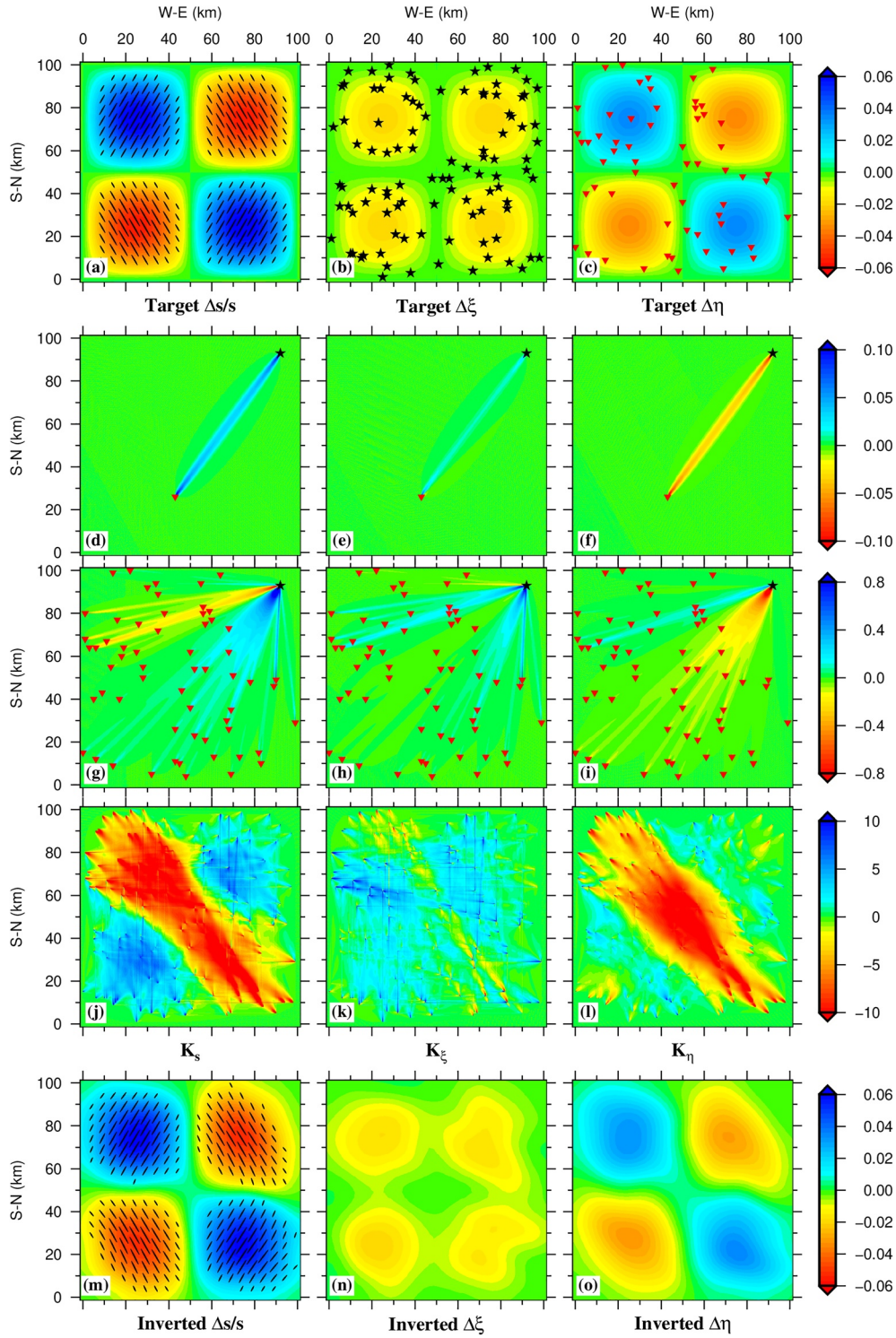
W-E (km)
S-N (km)
(a)
(b)
(c)
(d)
(e)
(f)
(g)
(h)
(i)
(j)
(k)
(l)
(m)
(n)
(o)
Target Δs/s
Target Δξ
Target Δη
K_s
K_ξ
K_η
Inverted Δs/s
Inverted Δξ
Inverted Δη

Figure 2.

can be expressed by $\left(s(\mathbf{x}),\xi(\mathbf{x}),\eta(\mathbf{x})\right) = \left(\frac{1}{6}\text{ s/km},0,0\right)$. The perturbations of the target model from the starting model are assumed to be

$$\frac{\Delta s(\mathbf{x})}{s(\mathbf{x})} = \frac{\Delta s(x,y,z)}{s(x,y,z)} = -\frac{6\% \cdot \sigma}{1 + 6\% \cdot \sigma}, \tag{27}$$

$$\Delta\xi(\mathbf{x}) = \Delta\xi(x,y,z) = 4\% \cdot |\sigma| \cos\left(\frac{2\pi\phi}{180}\right), \tag{28}$$

$$\Delta\eta(\mathbf{x}) = \Delta\xi(x,y,z) = 4\% \cdot |\sigma| \sin\left(\frac{2\pi\phi}{180}\right), \tag{29}$$

where

$$\sigma(x,y,z) = \sin\left(\frac{2\pi x}{100}\right)\sin\left(\frac{2\pi y}{100}\right), \qquad \phi = \begin{cases} 120°, & \text{if } \sigma > 0; \\ 60°, & \text{if } \sigma < 0. \end{cases} \tag{30}$$

Individual kernels (Figures 2d–2f), event kernels (Figures 2g–2i) and misfit kernels (Figures 2j–2l) are computed in the starting model. As suggested by Equations 14–17, the signs (colors) of these kernels are determined by the traveltime residual $T_n(\mathbf{x}) - T_n^o(\mathbf{x}_{r,m})$ at every related seismic station and the traveltime gradient $\nabla T_n(\mathbf{x})$. Five sets of regular grid evenly staggered along the diagonal direction (Figure S1) are used to discretize the relative slowness perturbation $\Delta s(\mathbf{x})/s(\mathbf{x})$ and the perturbations in $\xi(\mathbf{x})$ and $\eta(\mathbf{x})$. After a total of 20 iterations, the perturbations in slowness and two anisotropic parameters are almost fully recovered (Figures 2m–2o). The success of this synthetic example justifies the adjoint-state traveltime tomography method for azimuthally anisotropic media.

3. Earthquake Relocation in Azimuthally Anisotropic Media

Seismic traveltime tomography using earthquake data always demands for precise earthquake locations. In this section an eikonal equation-based earthquake location method is developed to provide the necessary tool for accurately locating earthquakes in azimuthally anisotropic media.

Assume that the first arrival of a discussing earthquake arrives at the seismic station $\mathbf{x}_{r,m}\,(m = 1,2,\ldots,M)$ at the time τ_m^o. $(\mathbf{x}_s,\tau)$ is the hypocenter of the earthquake. To relocate the hypocenter, we attempt to minimize the following objective function

$$\chi\left(\mathbf{x}_s,\tau\right) = \sum_{m=1}^{M} \frac{\omega_m}{2}\left[T(\mathbf{x}_{r,m}) - \left(\tau_m^o - \tau\right)\right]^2, \tag{31}$$

where $T(\mathbf{x})$ is the solution of the azimuthally anisotropic eikonal equation with the auxiliary condition $T(\mathbf{x}_s) = 0$. We further assume that $T_m(\mathbf{x})$ is the solution of the azimuthally anisotropic eikonal equation with the auxiliary condition $T_m(\mathbf{x}_{r,m}) = 0$. The principle of reciprocity says that the traveltime of a particular seismic phase from the earthquake location $\mathbf{x}_s$ to the seismic station $\mathbf{x}_{r,m}$ is the same as the traveltime from the seismic station $\mathbf{x}_{r,m}$ to the earthquake location $\mathbf{x}_s$ (Aki & Richards, 2002), that is, $T(\mathbf{x}_{r,m}) = T_m(\mathbf{x}_s)$. The objective function (31) can be alternatively expressed by

$$\chi\left(\mathbf{x}_s,\tau\right) = \sum_{m=1}^{M} \frac{\omega_m}{2}\left[T_m(\mathbf{x}_s) - \left(\tau_m^o - \tau\right)\right]^2. \tag{32}$$

If there is an infinitesimal perturbation $(\delta\mathbf{x}_s,\delta\tau)$ in $(\mathbf{x}_s,\tau)$, then the corresponding perturbation in the objective function (32) is

Figure 2. (a) The relative slowness perturbation of the target model from the starting model, $\Delta s(\mathbf{x})$ / $s(\mathbf{x})$. The black lines show the fast *P*-wave velocity directions of the target model. (b) The perturbation of the target model from the starting model in the anisotropic parameter $\xi(\mathbf{x})$. Black stars denote 100 earthquakes. (c) The perturbation of the target model from the starting model in the anisotropic parameter $\eta(\mathbf{x})$. Red inverse triangles represent 60 seismic stations. (d–f) sequentially show individual kernels $K_s(\mathbf{x})$, $K_\xi(\mathbf{x})$ and $K_\eta(\mathbf{x})$ corresponding to one pair of earthquake and seismic station. (g–i) display event kernels associated with the same earthquake as in (d–f). Traveltime residuals at all the 60 seismic stations contribute to the event kernels. (j–l) demonstrate the misfit kernels related to all the 100 earthquakes and 60 seismic stations. (m–o) show the inverted relative slowness perturbation $\Delta s(\mathbf{x})/s(\mathbf{x})$, the inverted $\Delta\xi(\mathbf{x})$ and the inverted $\Delta\eta(\mathbf{x})$. The color scales for the relative slowness perturbation, the perturbations in the two anisotropic parameters and the sensitivity kernels are on the right hand side of the respective plots. The units for the sensitivity kernels are uniformly $s^2 \cdot km^{-3}$. The perturbations $\Delta s(\mathbf{x})/s(\mathbf{x})$, $\Delta\xi(\mathbf{x})$ and $\Delta\eta(\mathbf{x})$ are unitless.

$$\delta\chi\left(\mathbf{x}_s,\tau\right)=\sum_{m=1}^{M}\omega_m\left[T_m(\mathbf{x}_s)-\left(\tau_m^o-\tau\right)\right]\left[\delta\mathbf{x}_s\cdot\nabla T_m(\mathbf{x}_s)+\delta\tau\right]. \tag{33}$$

At the minimizer $(\hat{\mathbf{x}}_s,\hat{\tau})$ the partial derivative of the objective function (32) with respect to the origin time is zero,

$$0=\frac{\partial\chi\left(\hat{\mathbf{x}}_s,\hat{\tau}\right)}{\partial\tau}=\sum_{m=1}^{M}\omega_m\left[T_m(\hat{\mathbf{x}}_s)-\left(\tau_m^o-\hat{\tau}\right)\right]. \tag{34}$$

Accordingly, at an estimated location $\mathbf{x}_s$ the optimal origin time can be approximated by

$$\hat{\tau}=\frac{\sum_{m=1}^{M}\omega_m\left[\tau_m^o-T_m(\mathbf{x}_s)\right]}{\sum_{m=1}^{M}\omega_m}. \tag{35}$$

Substituting Equation 35 into Equation 33, we have

$$\frac{\partial\chi\left(\mathbf{x}_s,\tau\right)}{\partial\mathbf{x}_s}=\sum_{m=1}^{M}\omega_m\left[T_m(\mathbf{x}_s)-\left(\tau_m^o-\hat{\tau}\right)\right]\nabla T_m(\mathbf{x}_s). \tag{36}$$

Equations 35 and 36 define the eikonal equation-based earthquake location method for azimuthally anisotropic media. Once the estimated origin time (35) and the gradient function (36) are computed, we use the step-size-controlled gradient descent method to find the optimal hypocenter in an iterative manner (Tong, 2021). A numerical experiment is conducted to show the correctness of the eikonal equation-based earthquake location algorithm for azimuthally anisotropic media (Text S1 and Figure S4), which also restates the importance of having full-azimuth data coverage and accurate velocity models for precise earthquake locations.

4. Azimuthal Anisotropy Tomography of Central California Near Parkfield

Previous studies using teleseismic receiver functions (Audet, 2015; Ozacar & Zandt, 2009; Porter et al., 2011) and shear wave splitting analysis of local earthquake data (Boness & Zoback, 2006; Yang et al., 2011) reveal that the upper, middle and lower crust around the San Andreas Fault (SAF) near Parkfield are characterized by strong anisotropy. To test the new tomography method and gain additional constraints on crustal seismic anisotropy from *P*-waves, the adjoint-state traveltime tomography method for azimuthally anisotropic media is applied to central California near Parkfield to image the anisotropic velocity structure of that region.

4.1. Tectonic Setting

The right-lateral strike-slip SAF is the transform boundary between the Pacific and North America plates (Figure 3). The Parkfield segment of the SAF is the transition zone between the creeping section of the SAF to the northwest and the locked section to the southeast (Ozacar & Zandt, 2009), where seven successive M_w ~6.0 earthquakes occurred at an average interval of 24.5 years since the 1857 Fort Tejon earthquake. The 2004 M_w 6.0 Parkfield earthquake is the most recent significant earthquake occurring in the transition zone (Figure 3). Near Parkfield the SAF separates the northeastern Franciscan Complex from the southwestern Salilian terrance (Figure 3) (Hole et al., 2001). The Franciscan Complex is composed of Late Cretaceous to early Tertiary mafic material and marine sedimentary rocks that accreted onto the North America plate (Audet, 2015), while the Salilian block is composed mainly of granitic and metamorphic rocks, which is believed to be largely a remnant Cretaceous arc underplated by lower-crust schists as a result of the oceanic Farallon plate subducting under the North America plate (Porter et al., 2011). Furthermore, as a key parameter reflecting the present-day state of tectonic stress, the axis of the maximum horizontal compressive stress S_{Hmax} in central California is reported to lie at a high angle to the SAF (Townend & Zoback, 2004).

4.2. Data and Initial Model

We have downloaded a total of about 2.44 million first *P*-wave arrivals with the associated earthquakes (magnitude > 1.0, occurring in a period from January 1984 to December 2020) and seismic stations located in the study area from Northern California Earthquake Data Center (NCEDC) and Southern California Earthquake Data Center (SCEDC) (NCEDC, 2014; SCEDC, 2013). All the first *P*-wave arrivals are inverted

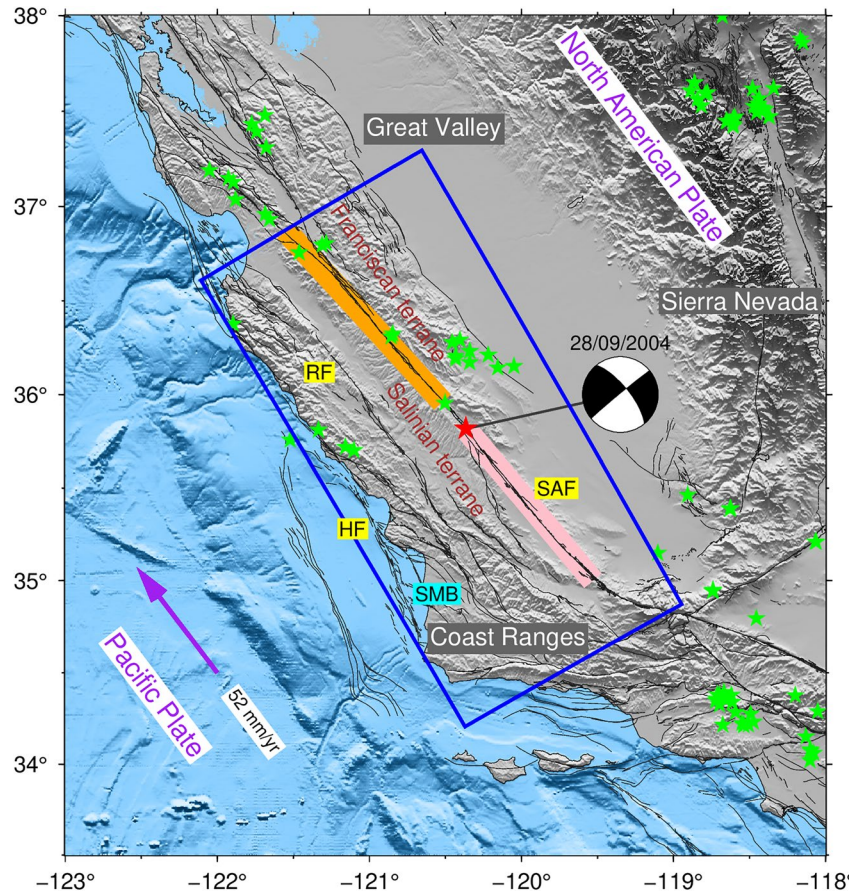

Figure 3. The tectonic setting and surface topography in central California. The red star together with the beach ball denotes the September 2004 M_w 6.0 Parkfield earthquake. The green stars are $M_w \geq 5.0$ earthquakes during the period from 1984 to 2020. The gray curves show the surface traces of active faults including the offshore Hosgri Fault (HF), the Rinconada Fault (RF) and the San Andreas Fault (SAF) (Jennings & Bryant, 2010). The creeping section of the SAF near Parkfiled is shaded in orange, the locked section is shaded in pink, and the middle segment is the transition zone (Lippoldt et al., 2017). SMB is short for Santa Maria Basin. Coast Ranges, Great Valley and Sierra Nevada are three geomorphic provinces in California. The purple arrow indicates the direction of the relative motion between the Pacific plate and the North American plate. The blue box outlines the study area of this work.

to obtain an optimal 1-D layered velocity model. Roughly following CRUST 1.0 for the Parkfield region (Laske et al., 2013), the 1-D layered model is separated by three discontinuities at depths of 4, 16, and 30 km. The *P*-wave velocities of the sedimentary layer, upper crust, lower crust and mantle are inverted to be 4.17, 6.03, 6.59, and 7.94 km/s, respectively. The flat discontinuity separating the crust from the mantle is then replaced by the curved Moho discontinuity extracted from CRUST 1.0 (Laske et al., 2013). After that, the three velocity contrasts in the depth direction are smoothed by convolving the 1-D velocity profile at every horizontal location with a 1-D Gaussian function (Tong et al., 2019). The 1-D Gaussian function with mean value 0.0 and standard deviation 0.4 km introduces a 2.4-km-thick transition zone at every velocity discontinuity. Finally, the initial model for *P*-wave azimuthal anisotropy tomography, denoted by $\mathbf{m}_0$, is constructed by choosing the smoothed isotropic velocity model as the average velocity component $\overline{v}(\mathbf{x})$ ($\overline{v}(\mathbf{x}) = 1/s(\mathbf{x})$) and setting the two anisotropic parameters $\xi(\mathbf{x}) = \eta(\mathbf{x}) = 0$.

The *P*-wave traveltime data are further filtered for the subsequent tomographic inversions and earthquake relocation. First, to avoid event clustering, we divide the study area into small blocks with a uniform size of 1 km by 1 km by 0.5 km and choose the only earthquake that has the maximum number of first *P*-wave arrivals from every block if there is any. Second, earthquake locations are adjusted according to the double-difference earthquake catalog for northern California (Waldhauser & Schaff, 2008) and the high-quality 1981–2019 waveform relocated earthquake catalog for southern California (Hauksson et al., 2012). Earth-

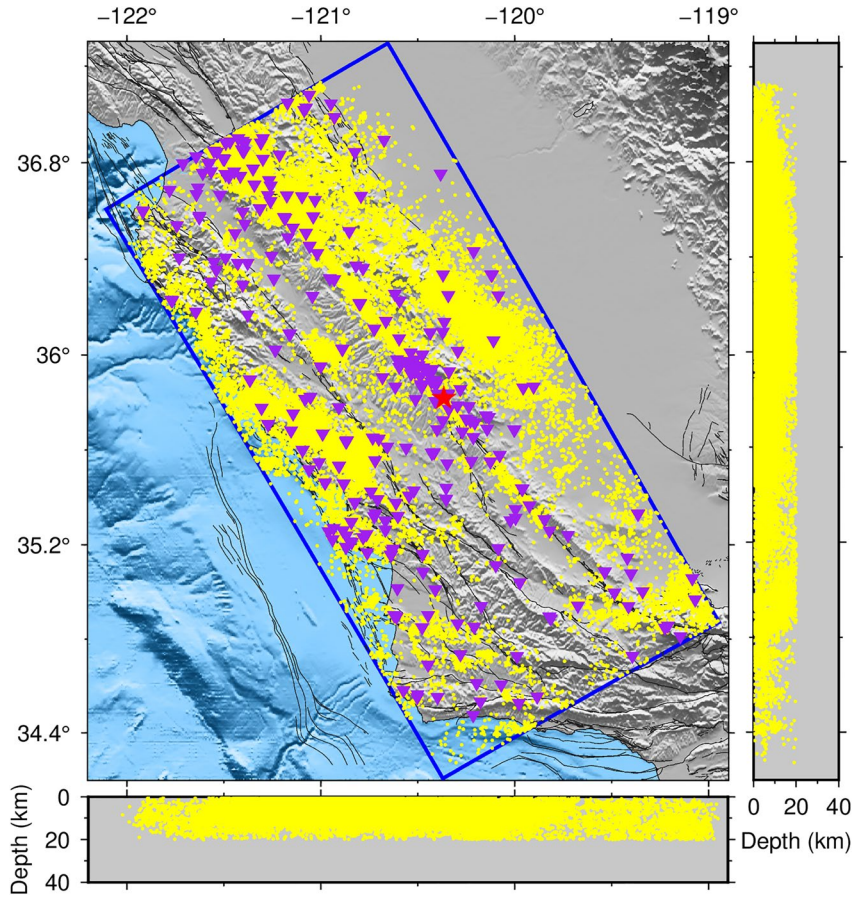

Figure 4. The spatial distributions of the 36,817 earthquakes (yellow dots) and 330 seismic stations (purple inverse triangles) selected for *P*-wave azimuthal anisotropy tomography using the adjoint-state method. The red star shows the epicenter of the 2004 M_w 6.0 Parkfield earthquake.

quakes not included in either catalog are not considered. Third, every selected earthquake must have a focal depth shallower than 20.0 km and have at least four first *P*-wave arrivals recorded in the study area. The main reason for excluding earthquakes deeper than 20 km depth is to reduce the influence of the Moho discontinuity and uppermost mantle velocity heterogeneity on the final crustal velocity model. Fourth, seismic stations having fewer than 4 first *P*-wave arrivals are removed. In total, we have selected 1,068,850 first *P*-wave arrivals of 36,817 earthquakes from 330 seismic stations (Figure 4). But if the absolute traveltime difference $\left|T_{obs} - T_{cal}\right|$ is greater than 5 s or the relative traveltime difference $\left|T_{obs}/T_{cal} - 1.0\right|$ is greater than 0.5, the associated *P*-wave arrival is ruled out from the tomographic inversion.

4.3. Resolution

Checkerboard resolution tests are performed to evaluate the resolving ability of the chosen *P*-wave data and the efficacy of the azimuthal anisotropy tomography method. The initial model is $\mathbf{m}_0$. The target checkerboard velocity model has perturbations in the average velocity $\overline{v}(\mathbf{x})$ and two anisotropic parameters $\xi(\mathbf{x}),\eta(\mathbf{x})$ with respect to the initial model. Mathematically, the perturbations can be expressed by

$$\frac{\Delta\overline{v}(\mathbf{x})}{\overline{v}(\mathbf{x})} = \frac{\Delta\overline{v}(x,y,z)}{\overline{v}(x,y,z)} = 8\% \cdot \sin\left(\frac{4\pi x}{310}\right)\sin\left(\frac{2\pi y}{150}\right)\sin\left(2\pi\frac{\sqrt{25+8z}-5}{8}\right), \tag{37}$$

$$\Delta\xi(\mathbf{x}) = \Delta\xi(x,y,z) = 8\% \cdot \left|\sigma\right|\cos\left(\frac{2\pi\phi}{180}\right), \tag{38}$$

$$\Delta\eta(\mathbf{x}) = \Delta\xi(x,y,z) = 8\% \cdot |\sigma| \sin\left(\frac{2\pi\phi}{180}\right), \tag{39}$$

where

$$\sigma(x,y,z) = \begin{cases} \sin\left(\frac{3\pi x}{310}\right)\sin\left(\frac{2\pi y}{150}\right)\sin\left(2\pi\frac{\sqrt{25+8z}-5}{8}\right), & \text{if } z < 7; \\ \sin\left(\frac{2\pi x}{310}\right)\sin\left(\frac{2\pi y}{150}\right)\sin\left(2\pi\frac{\sqrt{25+8z}-5}{8}\right), & \text{otherwise,} \end{cases} \tag{40}$$

$$\phi = \begin{cases} 150°, & \text{if } \sigma > 0; \\ 60°, & \text{if } \sigma < 0. \end{cases} \tag{41}$$

Note that the study area has a length of 310 km parallel to the SAF (x-axis) and a width of 150 km in the southwest-northeast direction (y-axis) (Figures 3 and 4). By substituting $z = 0,7,18$ or $z = 3,12,25$ into Equations 37 and 40, we can find that the target model has no perturbations at 0, 7, and 18 km depth and attain peak perturbations at depths of 3, 12, and 15 km. If we define the wavelength of the sinusoidal anomaly along a specific direction as the distance between two neighboring peaks in that direction, then the perturbations in $\overline{v}(\mathbf{x})$, $\xi(\mathbf{x})$ and $\eta(\mathbf{y})$ have the same wavelength of 150 km along the y-axis, the average velocity perturbation has a wavelength of 155 km along the x-axis, and the perturbations in $\xi(\mathbf{x})$ and $\eta(\mathbf{y})$ have the same wavelength of ~207 km above 7 km depth or 310 km below 7 km depth in the x-direction.

To recover the azimuthally anisotropic checkerboard velocity model, a multiple-grid consisting of eight spatially staggered regular grids (Figure S2) is used to discretize $\Delta\overline{v}(\mathbf{x})/\overline{v}(\mathbf{x})$. The spacing of every regular grid is adjusted based on the size of the anomaly. In principle, one wavelength anomaly is sampled by at least five nodes of a single regular grid to avoid spatial aliasing. Vice versa, based on the degree of recovery, the sizes of the checkerboard velocity anomalies should be increased or decreased to match (reflect) the resolving ability of the data. Admittedly, selecting eight sets of component grids to form the multiple-grid involves subjectivity. But from our previous experiences we generally find that the tomographic results remain almost the same when the number of component grids is greater than four (Tong et al., 2019). Another consideration is the density of the inversion nodes. The spacing of every component grid is about 39 km in the x-direction, and hence the multiple-grid with eight component grids places a node roughly every 5 km along the x-direction (Figure S2). As a result, the study area is densely sampled by the inversion nodes, which is helpful for recovering a high-resolution velocity model. Likewise, another similar multiple-grid consisting of eight regular grids (Figure S3) is chosen to discretize $\Delta\xi(\mathbf{x})$ and $\Delta\eta(\mathbf{x})$. To simulate picking errors existing in the real data, gaussian noise with average 0.0 s and standard deviation 0.05 s is added to the "observed" traveltimes calculated in the checkerboard velocity model. The anisotropic eikonal Equation 11 and its adjoint (17) are numerically solved on a dense forward grid with a dimension of $\Delta x = 0.6$ km by $\Delta y = 0.6$ km by $\Delta z = 0.2$ km at each iteration. No explicit damping and smoothing regularization techniques are applied. In spite of that, the perturbations are not allowed to exceed $\pm$ 2% at every iteration by using the step-size-controlled gradient descent method, and the multiple-grid consisting of eight relatively coarse regular grids also has a smoothing effect on the inversion results. The anisotropic velocity anomalies are largely recovered during the first 10 iterations, and the results become nearly unchanged after 30 iterations. We stop the inversion process at the 40-th iteration and consider $\mathbf{m}_{40}$ as the final model. It is necessary to mention that the new adjoint-state traveltime tomography method for seismic azimuthal anisotropy is computationally affordable and efficient, which requires a total of 2001 central processing unit (CPU) hours to finish the 40 iterations.

The checkerboard velocity model is satisfactorily recovered (Figures 5 and 6), indicating that the chosen P-wave traveltime data can resolve comparable azimuthally anisotropic velocity anomalies by using the new adjoint-state traveltime tomography method. In a local area north of the 2004 Parkfield mainshock, the anisotropic velocity structure from near the surface to about 14 km depth are well constrained (Figures 5a–5g and 6a–6g). At depths deeper than 10 km and around the southern end of the study area, probably due to the low seismicity there (Figure 4), the anomalous structures of the average velocity and two anisotropic

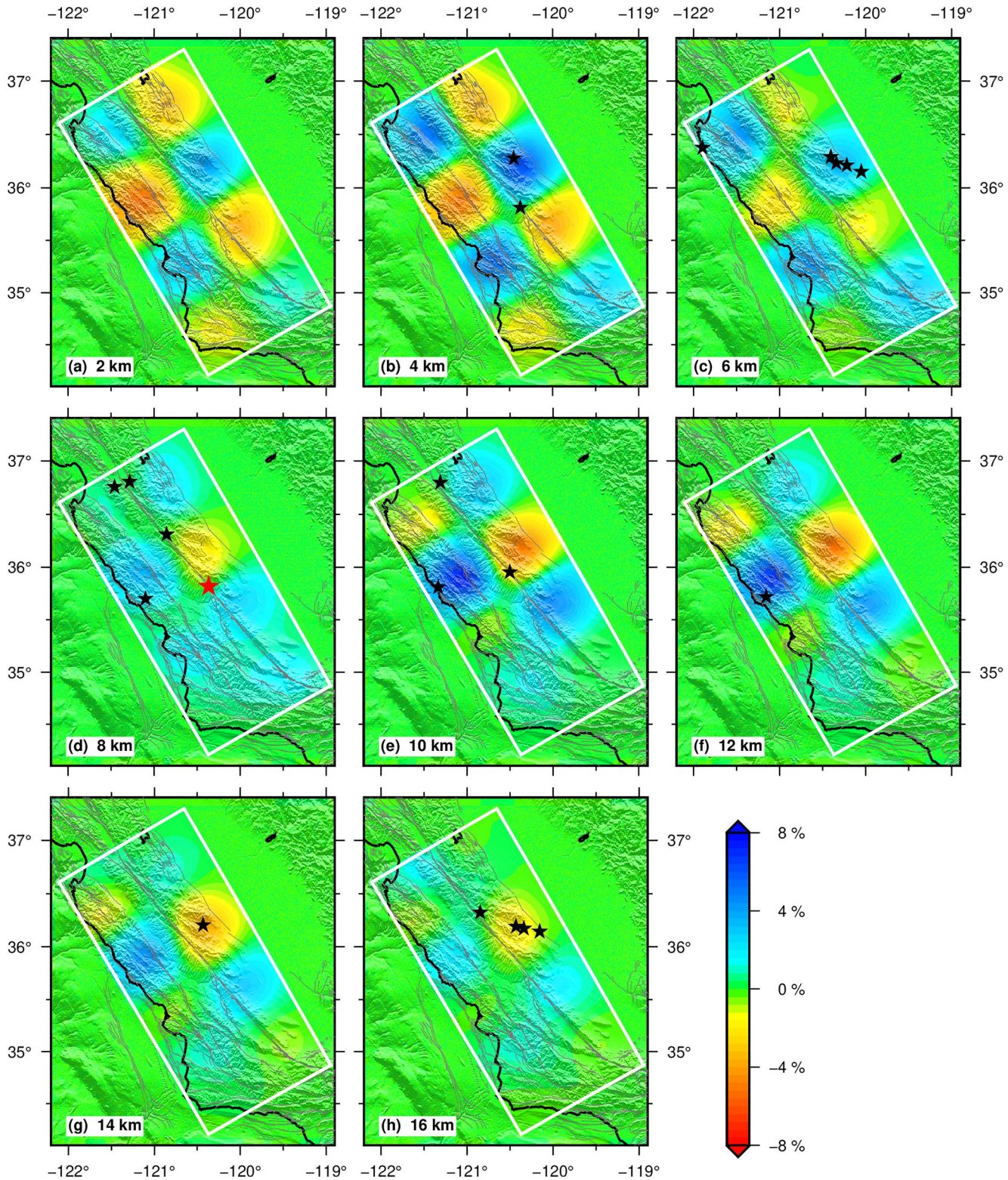

Figure 5. The results of the checkerboard resolution test for *P*-wave azimuthal anisotropy tomography solved by the adjoin-state method. The inverted relative velocity perturbations at 8 representative depths are shown. The red and blue colors denote negative and positive velocity perturbations, respectively. The color scale for the relative velocity perturbation is included at the bottom right corner. The red star is the 2004 M_w 6.0 Parkfield earthquake with a focal depth of ~8 km. The other black stars denote $M_w > 5.0$ earthquakes occurring during the period from 1984 to 2000, which are projected to their nearest horizontal slices.

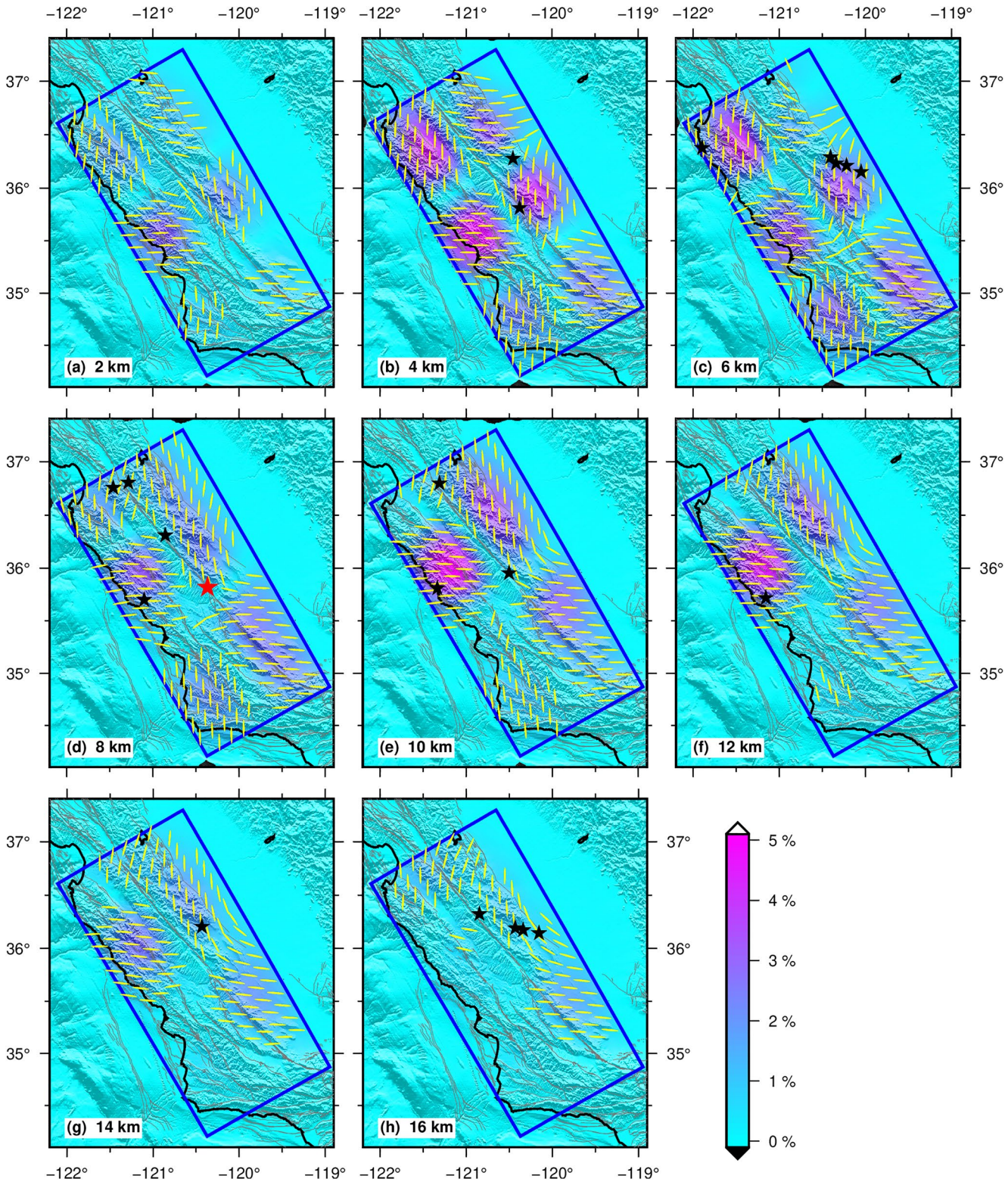

Figure 6. The results of the checkerboard resolution test for *P*-wave azimuthal anisotropy tomography solved by the adjoin-state method. As a continuation of Figure 5, the amplitudes and fast velocity directions of the recovered azimuthal anisotropy at eight representative depths are displayed. The yellow lines align with the fast *P*-wave velocity directions. The color scale for the amplitude of *P*-wave azimuthal anisotropy is placed at the bottom right corner.

parameters are poorly constrained (Figures 5f–5h and 6f–6h). Two additional checkerboard resolution tests are conducted to examine the coupling effect between seismic heterogeneity and seismic anisotropy. In comparison with the initial model $\mathbf{m}_0$, one checkerboard velocity model only has perturbations in the average velocity (Equation 37), and the other checkerboard velocity model only has perturbations in the two anisotropic parameters (Equations 38 and 39). But the three model parameters $\overline{v}(\mathbf{x})$, $\xi(\mathbf{x})$ and $\eta(\mathbf{x})$ are simultaneously determined. As displayed in Figures S5–S8, the leakage from seismic heterogeneity to seismic anisotropy or from seismic anisotropy to seismic heterogeneity is minor, implying that the chosen large amount of *P*-wave traveltime data can efficiently resolve and decouple seismic heterogeneity and seismic azimuthal anisotropy.

4.4. Results

The tomographic results are generated following a three-stage workflow. In the first stage, we develop an intermediate azimuthally anisotropic velocity model by iteratively refining the initial model $\mathbf{m}_0$ 30 times via the direction inversion of the chosen *P*-wave traveltimes (Figures S9 and S10). The accuracy of the intermediate velocity model is partly supported by the accuracy of earthquake hypocenters, which is in accordance with two high-quality earthquake catalogs mentioned in Section 4.2. In the second stage, all the 36,817 earthquakes are relocated in the intermediate anisotropic velocity model (Figures S9 and S10). The earthquake location algorithm has iterated 10 times. The *P*-wave traveltimes are also updated according to the relocated earthquake locations. In the third stage, starting again with the initial model $\mathbf{m}_0$, the updated *P*-wave traveltimes are inverted to develop an optimal azimuthally anisotropic velocity model. The iterative process stops after 30 iterations. In the three-stage workflow, we stop each iterative inversion process when the reduction in the objective function is less than 4.0% of the reduction amount at the first iteration. The CPU times used in the three stages are 1016, 38, and 1071 hr, respectively. Map views of the final average velocity and azimuthal anisotropy models at 8 representative depths are shown in Figures 7 and 8.

4.4.1. Average Velocity Model

The most striking feature of the average velocity model is the strong velocity contrast across the transition to the north creeping section of the SAF. On the northeast side of the SAF is the low-velocity Franciscan terrance and Great Valley Sequence, and on the southwest of the SAF is the high-velocity Salinian terrance. The velocity contrast persists from the surface to a depth of about 14 km. As a well-known feature in central California, many previous studies have identified this sharp lateral velocity contrast across the SAF (on the order of 1 km/s) (e.g., Eberhart-Phillips & Michael, 1993; Lippoldt et al., 2017; Thurber et al., 2006; Zeng et al., 2016). The sharp velocity contrast is a key factor that affects the slip behavior of the SAF near Parkfield (Piana Agostinetti et al., 2020). Regarding the locked section of the SAF south of Parkfield, the *P*-wave velocity of the Great Valley east of the SAF is still lower than that of the Coast Ranges west of the SAF at shallow depths (Figure 7a). But in the middle crust the east side has a higher *P*-wave velocity than the west (Figures 7f–7h). The mid-crustal high-velocity structure probably reflects the gently southwest-dipping Great Valley ophiolite body (Liu & Tong, 2021; Thurber et al., 2009).

There is a second significant low-velocity anomaly near the coast at about 35° north, which extends from the surface to at least mid-crustal depths. The shallow part of this low-velocity anomaly is directly related to the sedimentary Santa Maria Basin and numerous northwest-southeast trending faults, including the offshore Hosgri Fault (Figures 7a and 7b). The root of the low-velocity Santa Maria Basin is connected to a deeper and larger low-velocity zone deviating slightly to the north (Figures 7c–7g). At 16 km depth, the low-velocity zone seems to meet with another broad low-velocity anomaly beneath the creeping section of the SAF (Figure 7h).

The broad mid-crustal low-velocity zone beneath the SAF trace is a continuation of the upper crustal low-velocity structure east of the SAF. Its expansion into the lower crust and uppermost mantle was clearly imaged by a recent ambient noise tomography study (Lippoldt et al., 2017). Additionally, the electrical resistivity model of the crust near Parkfield derived from magnetotelluric data suggests a high-conductivity zone penetrating the entire crust (Becken et al., 2011). The high-conductivity zone is interpreted to be a deep-rooted channel for crustal and/or mantle fluids (Becken et al., 2011). Lippoldt et al. (2017) reported that the high-conductivity zone coincides with the upper crustal, lower crustal and uppermost mantle low-velocity anomalies beneath the SAF near Parkfield. Thus, the crustal low-velocity structures consistently imaged by the present and previous studies suggest the presence of fluids and moreover, crustal fluids may have played

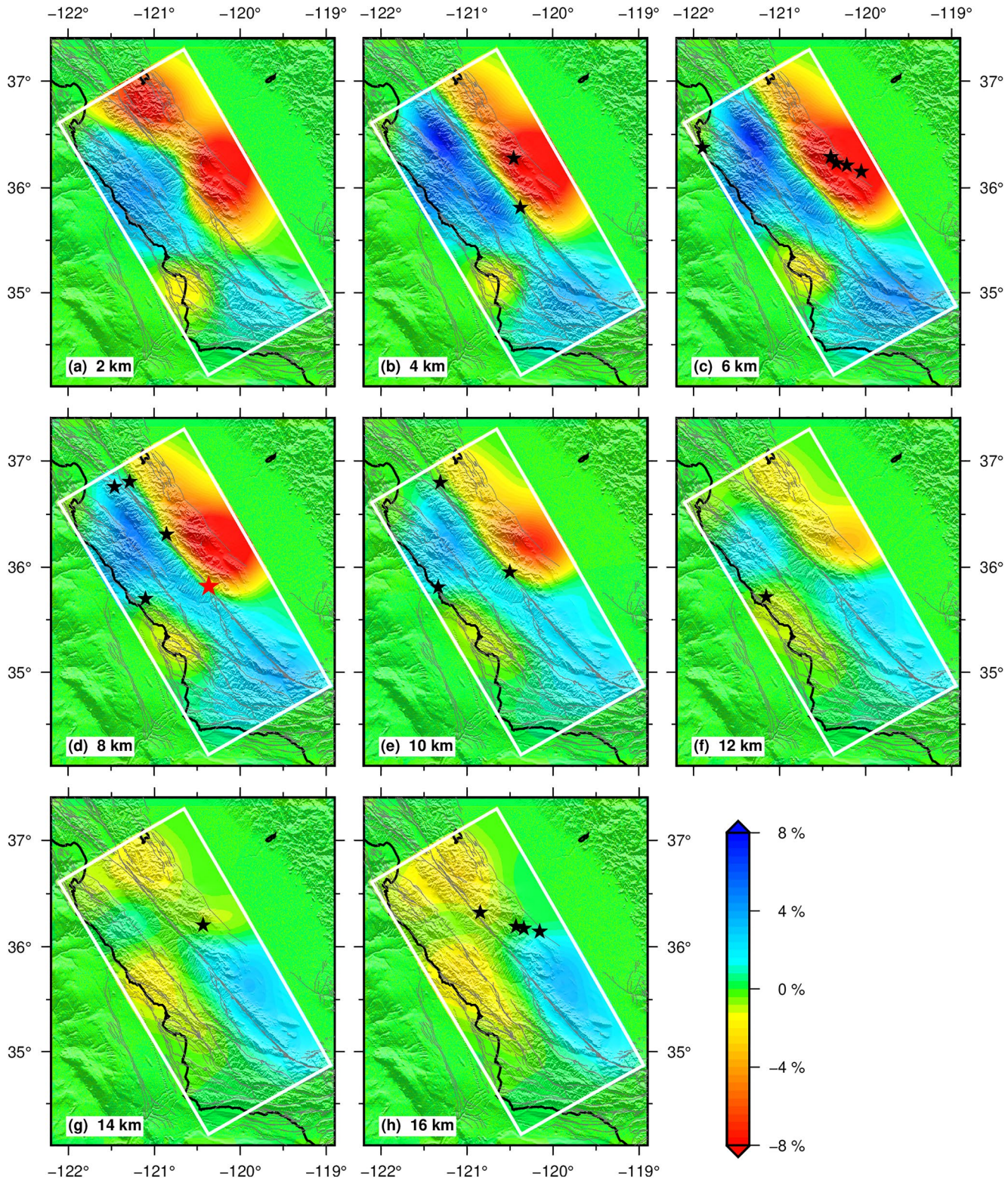

Figure 7. The relative perturbation of the average velocity generated by adjoint-state traveltime tomography for azimuthally anisotropic media using real data. All the others are same as Figure 5.

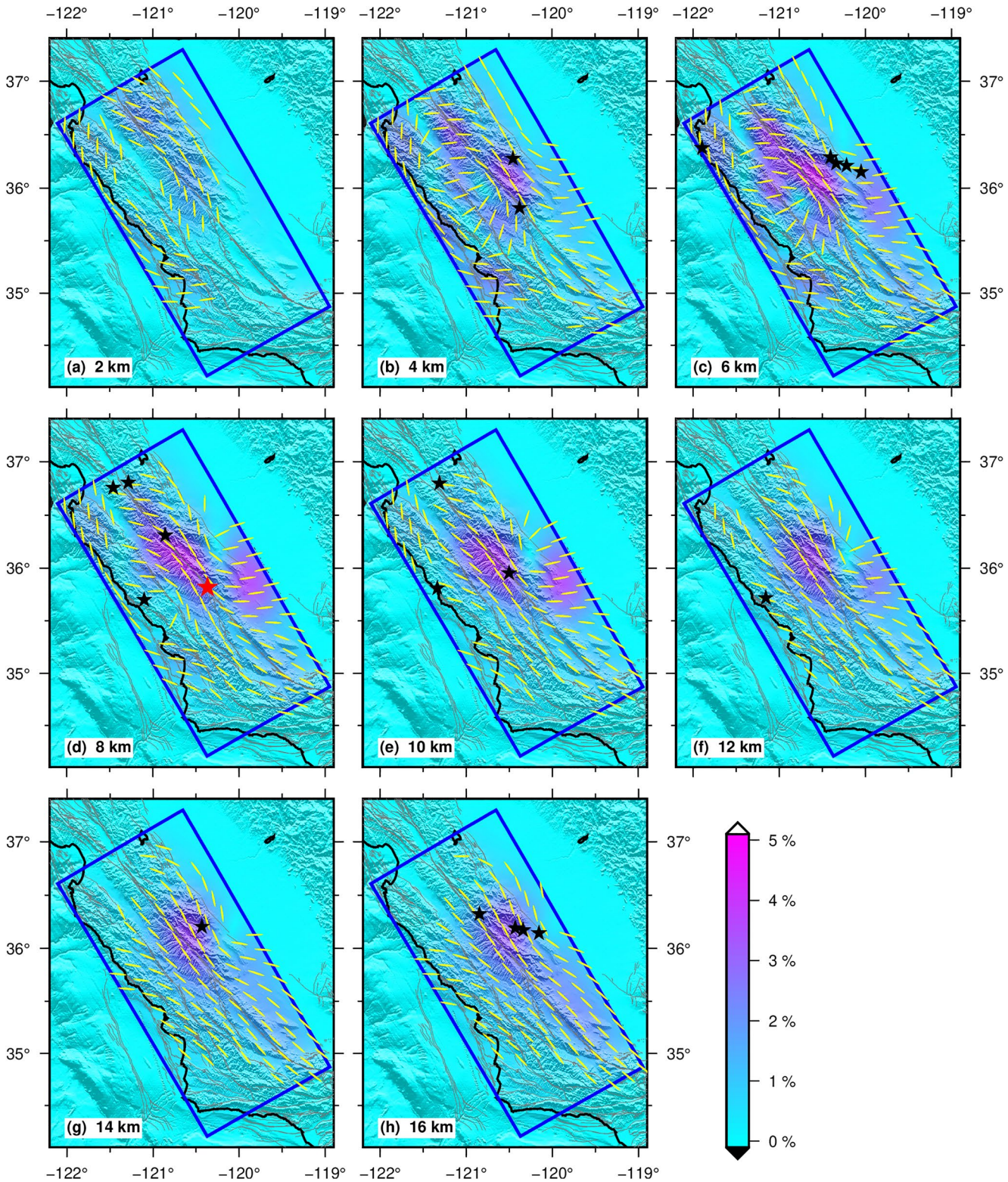

Figure 8. The amplitude and fast velocity direction of the azimuthal anisotropy in the study area revealed by adjoint-state traveltime tomography for azimuthally anisotropic media using real data. All the others are same as Figure 6.

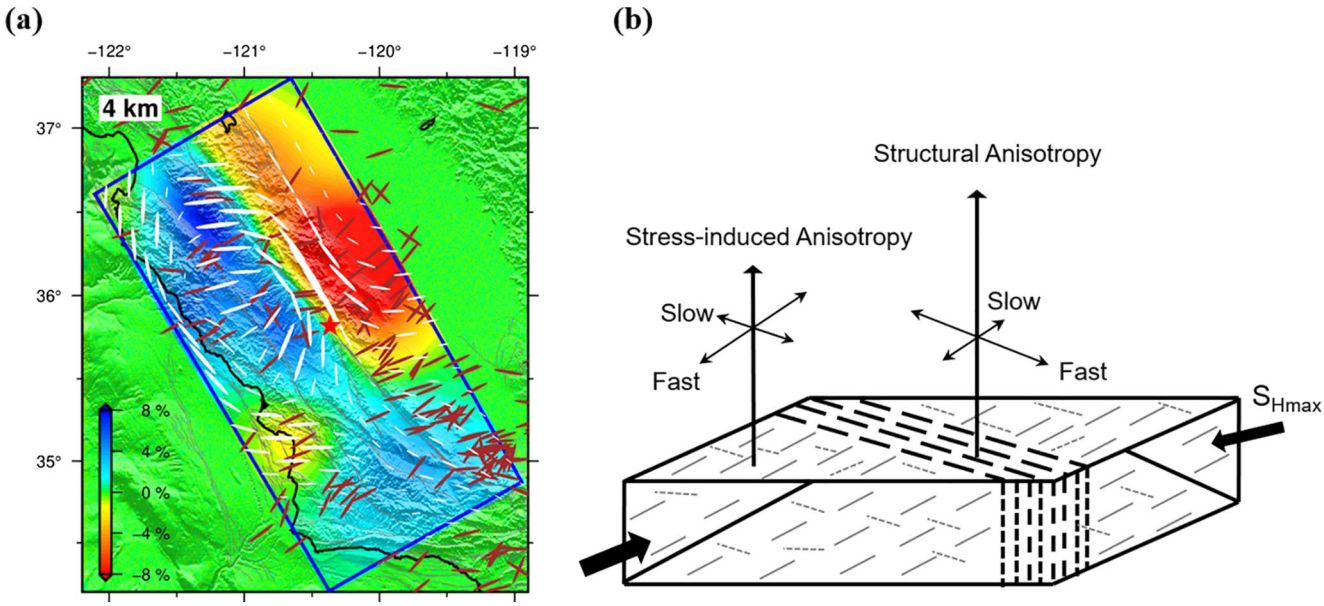

Figure 9. (a) The relative perturbation of the average velocity together with the fast *P*-wave velocity directions (white lines) at 4 km depth as generated by the adjoint-state traveltime tomography method for azimuthally anisotropic media. The amplitude of the azimuthal anisotropy is proportional to the length of the white line. The purple lines show the directions of the maximum horizontal compressive stress S_{Hmax} (Heidbach et al., 2016). The color scale for the relative velocity perturbation is included at the bottom left corner. The red star is at the epicenter location of the 2004 M_w 6.0 Parkfield earthquake. (b) A schematic diagram illustrating structural anisotropy in the fault zone and stress-induced anisotropy adjacent to (but not on) the fault. Off the fault zone, the fast velocity directions are parallel to S_{Hmax}. Within the fault zone, the fast velocity direction is parallel to fault fabric. This diagram is modified from Figure 1 of Boness and Zoback (2006).

an important role in the generation of earthquakes and tremors in the Parkfield region (Becken et al., 2011; Lippoldt et al., 2017; Zeng et al., 2016).

4.4.2. Azimuthal Anisotropy

The azimuthal anisotropy model reveals pervasive crustal seismic anisotropy in the study area (Figure 8). Along the trace of the SAF, the fast *P*-wave velocity directions generally follow the northwest-southeast trend of the SAF, indicating that seismic anisotropy in the San Andreas Fault zone is mostly structure-induced. Similarly, in the region west of the locked section of the SAF, the fast *P*-wave velocity directions align with the strikes of the faults, suggesting again that structural anisotropy is the main mechanism for seismic anisotropy due to the presence of faults there. Structure-induced seismic anisotropy is observable not only in the upper crust (Figures 8a–8d) but also in the middle crust (Figures 8e–8h). Particularly beneath and to the west of the SAF, the uniform northwest-southeast trend of anisotropic fabric in the middle crust coincides with the direction of the relative motion between the Pacific and North American plates (Figures 8e–8h). This phenomenon implies that the mid-crustal rocks are possibly sustaining substantial shear stresses (Behr & Platt, 2014). The deep extension of the SAF to ~50 km imaged by ambient noise data (Lippoldt et al., 2017) and evidence of low-frequency earthquakes occurring in the SAF zone at depths from 18 to 28 km (Zeng et al., 2016) suggest the existence of ductile shear zones, as a result of the shear stresses, in the mid-lower crust (Shelly et al., 2009).

However, structure-induced anisotropy is not the only mechanism for seismic anisotropy in the study area. To the west of the transition to creeping section of the SAF, the fast directions in the upper crust have high angles (> 45°) to the Rinconada Fault and SAF (Figures 8b–8d). To the east of Parkfield within the Great Valley, the northeast-southwest-oriented fast directions are nearly perpendicular to the SAF (Figures 8b–8f). Not parallel to the active faults (Figure 9a), the fast velocity directions in the two local areas are consistent with the uniform NNE-SSW orientation of the maximum horizontal compressional stress S_{Hmax} in central California (Townend & Zoback, 2004). Therefore, we infer that upper crustal seismic anisotropies of the two specific local areas are mainly stress-induced.

By analyzing *S*-wave splitting measurements from local earthquakes in California, Boness and Zoback (2006) find that the maximum horizontal compressive stress S_{Hmax} at seismic stations adjacent to (but not on) the SAF is at a high angle to the strike of the fault and fast shear waves inside fault zones are parallel to fault fabric (Figure 9b). *P*-wave traveltime data of local earthquakes reveal the same pattern of seismic anisotropy in the upper crust around the transition to creeping section of the SAF (Figures 8b–8d). Teleseismic receiver functions from a local seismic network near Parkfield indicate that the fast axis of seismic anisotropy is parallel to the main strike of the SAF over an area of ~100 km^2 (Audet, 2015). This is consistent with the finding of the present study. In addition, our results show that seismic anisotropy is more prominent along the transition to creeping section of the SAF (Figure 8).

5. Discussion and Conclusions

We have derived an anisotropic eikonal equation to simulate the first-arrival traveltime field in azimuthally anisotropic media with mirror symmetry. That particular anisotropic eikonal Equation 11 involves three model parameters including the average slowness $s(\mathbf{x})$ and two anisotropic parameters $\xi(\mathbf{x})$ and $\eta(\mathbf{x})$ or equivalently the average slowness $s(\mathbf{x})$, the magnitude of anisotropy $\epsilon(\mathbf{x})$, and the fast velocity direction $\phi(\mathbf{x})$. The anisotropic eikonal equation-constrained optimization problem to match the observed traveltimes with calculated traveltimes can be solved by the efficient adjoint-state method. The sensitivity kernels of the objective function with respect to $s(\mathbf{x})$, $\xi(\mathbf{x})$ and $\eta(\mathbf{x})$ are formulated in terms of the forward traveltime field and an adjoint field. The adjoint field satisfies the transport-type adjoint equation. It transports the traveltime residuals observed at seismic receiver locations back to the source location and subsequently finds the contribution of every point in the space to the traveltime residuals. After numerically solving the anisotropic eikonal equation and the adjoint equation, we can obtain the values of the objective function and sensitivity kernels. The multiple-grid model parameterization is used to discretize the anisotropic velocity model. Following that, the step-size-controlled gradient descent method is adopted to find the optimal azimuthally anisotropic velocity model in an iterative manner. Typically different from previous seismic anisotropic tomography studies, neither ray tracing nor computationally expensive wavefield modeling is needed by the adjoint-state traveltime tomography method. In particular, due to the increased complexity of ray tracing in anisotropic media, it was quite common to trace ray paths in the isotropic average velocity model by assuming that weak seismic anisotropy has little influence on ray paths (e.g., Eberhart-Phillips & Henderson, 2004; Liu & Tong, 2021). This assumption is no longer required for the adjoint-state traveltime tomography method. In addition, an eikonal equation-based earthquake location method is developed to locate earthquakes in azimuthally anisotropic media.

From the methodological perspective, the adjoint-state traveltime tomography method and eikonal equation-based earthquake location method for azimuthally anisotropic media of this study are sophisticated extensions of the ones for isotropic media discussed in Tong (2021). They inherit all the advantages and drawbacks of their isotropic counterparts. For instance, all the eikonal equation-based methods require moderate computational resources and can be operated on moderately equipped desktop workstations of nowadays (Tong, 2021). When there are more earthquakes than seismic stations, the tomography methods for both isotropic and anisotropic media can treat seismic stations as "virtual" earthquakes and earthquakes as "virtual" stations to save computational cost. But the success of seismic anisotropy tomography has a higher requirement for the azimuthal distribution of seismic data.

In the study area of central California near Parkfield, both structural and stress-induced seismic anisotropy are observed in the upper and middle crust. The predominant fault-parallel fast velocity directions suggest that the alignment of macroscopic fractures is the main cause for seismic anisotropy in the upper and middle crust (Boness & Zoback, 2006). The pervasive structural anisotropy has an excellent correlation with the numerous strike-slip faults west of the SAF. Stress-induced seismic anisotropy is observed at two places: One is west of the transition to creeping section of the SAF, mainly in the upper crust; the other is east of the SAF, in the upper to middle crust beneath the Great Valley. The fast *P*-wave velocity directions at the two places are consistent with the uniform NNE-SSW orientation of the maximum horizontal compressional stress S_{Hmax}. Following Boness and Zoback (2006), we consider that the preferential closure of fractures in response to the tectonic stress is the main cause for seismic anisotropy there. In brief, the upper crust seismic anisotropy indicated by the fast *P*-wave velocity directions (Figures 8a–8d) can be well explained by the schematic model derived from shear-wave splitting data (Figure 9b), which describes structural anisotropy

in the fault zone and stress-induced anisotropy off but adjacent to the fault zone. As the depth increases, the increasing confining pressure reduces the influence of the S_{Hmax} on anisotropy (Boness & Zoback, 2006; Liu & Tong, 2021), leaving mainly fault-parallel fast *P*-wave velocity directions in the middle crust (Figures 8e–8h). Regarding velocity heterogeneity, the striking feature that the SAF separates the low-velocity Franciscan terrance on the east from the high-velocity Salinian block on the west is clearly imaged.

In conclusion, the eikonal equation-based earthquake location method for azimuthally anisotropic media can precisely locate earthquakes with high accuracy by taking into account the effect of seismic anisotropy; while the adjoint-state seismic azimuthal anisotropy tomography method provides a new, accurate and powerful tool to continuously map seismic anisotropic structure of the Earth's interior.

Appendix A: Sensitivity Kernels

An infinitesimal perturbation $\left(\delta s(\mathbf{x}),\delta\xi(\mathbf{x}),\delta\eta(\mathbf{x})\right)$ in the azimuthally anisotropic velocity model $\left(s(\mathbf{x}),\xi(\mathbf{x}),\eta(\mathbf{x})\right)$ causes an infinitesimal perturbation $\delta T_n(\mathbf{x}_{r,m})$ in the calculated traveltime $T_n(\mathbf{x}_{r,m})$. The resultant perturbation in the objective function (12) can be approximated by

$$\begin{aligned}\delta\chi\left(s(\mathbf{x})\right) &= \sum_{n=1}^{N}\sum_{m=1}^{M}\omega_{n,m}\left[T_n(\mathbf{x}_{r,m})-T_n^o(\mathbf{x}_{r,m})\right]\delta T_n(\mathbf{x}_{r,m})\\ &= \sum_{n=1}^{N}\int_\Omega\sum_{m=1}^{M}\omega_{n,m}\left[T_n(\mathbf{x})-T_n^o(\mathbf{x}_{r,m})\right]\delta T_n(\mathbf{x})\delta(\mathbf{x}-\mathbf{x}_{r,m})d\mathbf{x}.\end{aligned} \tag{A1}$$

In the perturbed anisotropic velocity model, the eikonal equation takes the form

$$\begin{gathered}\left[\nabla(T_n+\delta T_n)\right]^t\begin{bmatrix}1+2(\xi+\delta\xi) & 2(\eta+\delta\eta) & 0\\ 2(\eta+\delta\eta) & 1-2(\xi+\delta\xi) & 0\\ 0 & 0 & 1+2\gamma\sqrt{(\xi+\delta\xi)^2+(\eta+\delta\eta)^2}\end{bmatrix}\\ \nabla(T_n+\delta T_n)=\left(s+\delta s\right)^2.\end{gathered} \tag{A2}$$

For compactness, the functional dependence on the spatial variable $\mathbf{x}$ is omitted. Subtracting Equation 11 from Equation A2 and ignoring second- and third-order terms, we have

$$\left[\nabla T_n\right]^t R\nabla\delta T_n=\left[\nabla T_n\right]^t\begin{bmatrix}-\delta\xi & -\delta\eta & 0\\ -\delta\eta & \delta\xi & 0\\ 0 & 0 & -\gamma\dfrac{\delta\xi+\delta\eta}{\sqrt{\xi^2+\eta^2}}\end{bmatrix}\nabla T_n+s\delta s, \tag{A3}$$

where

$$R=\begin{bmatrix}1+2\xi & 2\eta & 0\\ 2\eta & 1-2\xi & 0\\ 0 & 0 & 1+2\gamma\sqrt{\xi^2+\eta^2}\end{bmatrix}. \tag{A4}$$

Multiply an arbitrary test function $P_n(\mathbf{x})$ on both sides of Equation A3 and integrate the Earth volume Ω,

$$\int_\Omega P_n\left[\nabla T_n\right]^t R\nabla\delta T_n d\mathbf{x}=\int_\Omega P_n\left[\nabla T_n\right]^t\begin{bmatrix}-\delta\xi & -\delta\eta & 0\\ -\delta\eta & \delta\xi & 0\\ 0 & 0 & -\gamma\dfrac{\delta\xi+\delta\eta}{\sqrt{\xi^2+\eta^2}}\end{bmatrix}\nabla T_n d\mathbf{x}+\int_\Omega P_n s\delta s d\mathbf{x}. \tag{A5}$$

The left hand side of Equation A5 is

$$\begin{aligned} LHS &= \int_\Omega P_n \left[\nabla T_n\right]^t R \nabla \delta T_n d\mathbf{x} \\ &= \int_\Omega \nabla \cdot \left\{P_n \left[\nabla T_n\right]^t R \delta T_n\right\} d\mathbf{x} - \int_\Omega \delta T_n \nabla \cdot \left\{P_n \left[\nabla T_n\right]^t R\right\} d\mathbf{x}, \end{aligned} \tag{A6}$$

which can be simplified to

$$LHS = \int_\Omega \delta T_n \nabla \cdot \left\{P_n \left[-\nabla T_n\right]^t R\right\} d\mathbf{x} \tag{A7}$$

by assuming $P_n(\mathbf{x}) = 0$ on the boundary $\partial\Omega$. Equating it to the right hand side of Equation A5 yields

$$\begin{aligned} \int_\Omega \delta T_n \nabla \cdot \left\{P_n \left[-\nabla T_n\right]^t R\right\} d\mathbf{x} &= \int_\Omega \left[\nabla T_n\right]^t \begin{bmatrix} -\delta\xi & -\delta\eta & 0 \\ -\delta\eta & \delta\xi & 0 \\ 0 & 0 & -\gamma \dfrac{\delta\xi + \delta\eta}{\sqrt{\xi^2 + \eta^2}} \end{bmatrix} \left[\nabla T_n\right] P_n d\mathbf{x} \\ &\quad + \int_\Omega P_n s \delta s d\mathbf{x}. \end{aligned} \tag{A8}$$

Now we make the second assumption about $P_n(\mathbf{x})$:

$$\begin{aligned} &\nabla \cdot \left\{P_n(\mathbf{x}) \left[-\nabla T_n(\mathbf{x})\right]^t \begin{bmatrix} 1 + 2\xi(\mathbf{x}) & 2\eta(\mathbf{x}) & 0 \\ 2\eta(\mathbf{x}) & 1 - 2\xi(\mathbf{x}) & 0 \\ 0 & 0 & 1 + 2\gamma\sqrt{\xi^2(\mathbf{x}) + \eta^2(\mathbf{x})} \end{bmatrix}\right\} \\ &= \sum_{m=1}^{M} \omega_{n,m} \left[T_n(\mathbf{x}) - T_n^o(\mathbf{x}_{r,m})\right] \delta(\mathbf{x} - \mathbf{x}_{r,m}), \end{aligned} \tag{A9}$$

where the matrix R and functional dependence on $\mathbf{x}$ are explicitly stated. As shown in Equation A9, $P_n(\mathbf{x})$ is generated by the transport of the traveltime misfit at every seismic station back to the earthquake location $\mathbf{x}_{s,n}$, along a direction given by $[-\nabla T_n(\mathbf{x})]^t R$. Equation A9 is the adjoint equation of the eikonal Equation 11. We call $P_n(\mathbf{x})$ the adjoint field.

Substituting Equation A9 in Equation A8, we obtain that

$$\begin{aligned} &\int_\Omega \delta T_n(\mathbf{x}) \left[\sum_{m=1}^{M} \omega_{n,m} \left[T_n(\mathbf{x}) - T_n^o(\mathbf{x}_{r,m})\right] \delta(\mathbf{x} - \mathbf{x}_{r,m})\right] d\mathbf{x} \\ &= \int_\Omega \left[\nabla T_n(\mathbf{x})\right]^t \begin{bmatrix} -\delta\xi(\mathbf{x}) & -\delta\eta(\mathbf{x}) & 0 \\ -\delta\eta(\mathbf{x}) & \delta\xi(\mathbf{x}) & 0 \\ 0 & 0 & -\gamma \dfrac{\delta\xi(\mathbf{x}) + \delta\eta(\mathbf{x})}{\sqrt{\xi^2(\mathbf{x}) + \eta^2(\mathbf{x})}} \end{bmatrix} \left[\nabla T_n(\mathbf{x})\right] P_n(\mathbf{x}) d\mathbf{x} \\ &\quad + \int_\Omega P_n(\mathbf{x}) s(\mathbf{x}) \delta s(\mathbf{x}) d\mathbf{x}. \end{aligned} \tag{A10}$$

Comparing Equation A10 with Equation A1, the infinitesimal perturbation in the objective function χ is directly related to the perturbations in $s(\mathbf{x})$, $\xi(\mathbf{x})$, and $\eta(\mathbf{x})$ as

$$\begin{aligned} \delta\chi\left(s(\mathbf{x}), \xi(\mathbf{x}), \eta(\mathbf{x})\right) &= \sum_{n=1}^{N} \int_\Omega P_n(\mathbf{x}) s^2(\mathbf{x}) \frac{\delta s(\mathbf{x})}{s(\mathbf{x})} d\mathbf{x} \\ &\quad + \sum_{n=1}^{N} \int_\Omega \left[\nabla T_n(\mathbf{x})\right]^t \begin{bmatrix} -1 & 0 & 0 \\ 0 & 1 & 0 \\ 0 & 0 & -\dfrac{\gamma}{\sqrt{\xi^2(\mathbf{x}) + \eta^2(\mathbf{x})}} \end{bmatrix} \nabla T_n(\mathbf{x}) P_n(\mathbf{x}) \delta\xi(\mathbf{x}) d\mathbf{x} \\ &\quad + \sum_{n=1}^{N} \int_\Omega \left[\nabla T_n(\mathbf{x})\right]^t \begin{bmatrix} 0 & -1 & 0 \\ -1 & 0 & 0 \\ 0 & 0 & -\dfrac{\gamma}{\sqrt{\xi^2(\mathbf{x}) + \eta^2(\mathbf{x})}} \end{bmatrix} \nabla T_n(\mathbf{x}) P_n(\mathbf{x}) \delta\eta(\mathbf{x}) d\mathbf{x}. \end{aligned} \tag{A11}$$

We can rewrite Equation A11 in terms of the traveltime misfit kernels

$$\delta\chi\left(s(\mathbf{x}),\xi(\mathbf{x}),\eta(\mathbf{x})\right) = \int_\Omega K_s(\mathbf{x})\frac{\delta s(\mathbf{x})}{s(\mathbf{x})}d\mathbf{x} + \int_\Omega K_\xi(\mathbf{x})\delta\xi(\mathbf{x})d\mathbf{x} + \int_\Omega K_\eta(\mathbf{x})\delta\eta(\mathbf{x})d\mathbf{x}, \tag{A12}$$

where

$$K_s(\mathbf{x}) = \sum_{n=1}^{N} P_n(\mathbf{x})s^2(\mathbf{x}), \tag{A13}$$

$$K_\xi(\mathbf{x}) = \sum_{n=1}^{N}\left[\nabla T_n(\mathbf{x})\right]^t \begin{bmatrix} -1 & 0 & 0 \\ 0 & 1 & 0 \\ 0 & 0 & -\dfrac{\gamma}{\sqrt{\xi^2(\mathbf{x})+\eta^2(\mathbf{x})}} \end{bmatrix} \nabla T_n(\mathbf{x})P_n(\mathbf{x}), \tag{A14}$$

$$K_\eta(\mathbf{x}) = \sum_{n=1}^{N}\left[\nabla T_n(\mathbf{x})\right]^t \begin{bmatrix} 0 & -1 & 0 \\ -1 & 0 & 0 \\ 0 & 0 & -\dfrac{\gamma}{\sqrt{\xi^2(\mathbf{x})+\eta^2(\mathbf{x})}} \end{bmatrix} \nabla T_n(\mathbf{x})P_n(\mathbf{x}). \tag{A15}$$

The traveltime misfit kernels $K_s(\mathbf{x})$, $K_\xi(\mathbf{x})$ and $K_\eta(\mathbf{x})$ represent the Fréchet derivatives with respect to the average slowness $s(\mathbf{x})$ and two anisotropic parameters $\xi(\mathbf{x})$ and $\eta(\mathbf{x})$, respectively. If the objective function (12) only involves one earthquake, the traveltime misfit kernels are also called event kernels (Tape et al., 2007; Tong, 2021). Specifically, the misfit kernels corresponding to one pair of earthquake and seismic station are individual kernels (Tong, 2021; Tromp et al., 2005).

Data Availability Statement

The seismic data are downloaded from the Northern California Earthquake Data Center (NCEDC, 2014) and Southern California Earthquake Data Center (SCEDC, 2013). Most figures are made with the Generic Mapping Tool (GMT) (Wessel & Smith, 1991).

Acknowledgments
The author thanks the Editor Yehuda Ben-Zion and the Associate Editor Andreas Fichtner for handing this paper. The author is grateful to Jean Virieux and another anomalous reviewer for their critical comments that have greatly improved the paper. This work is supported by the Minister of Education, Singapore, under its MOE AcRF Tier-2 Grant (04MNP002073C230). This work comprises Earth Observatory of Singapore contribution no. 367. This research is also partly supported by the National Research Foundation Singapore and the Singapore Ministry of Education under the Research Centers of Excellence Initiative (Project Code Number: 04MNS001953A620).

References

Aki, K., & Richards, P. G. (2002). *Quantitative seismology: Theory and methods* (2nd ed.). University Science Books.
Audet, P. (2015). Layered crustal anisotropy around the San Andreas Fault near Parkfield, California. *Journal of Geophysical Research: Solid Earth*, *120*, 3527–3543. https://doi.org/10.1002/2014jb011821
Bar, N., Long, M. D., Wagner, L. S., Beck, S. L., Zandt, G., & Tavera, H. (2019). Receiver function analysis reveals layered anisotropy in the crust and upper mantle beneath southern Peru and northern Bolivia. *Tectonophysics*, *753*, 93–110. https://doi.org/10.1016/j.tecto.2019.01.007
Basu, U., & Powell, C. (2019). Pn tomography and anisotropy study of the central United States. *Journal of Geophysical Research: Solid Earth*, *124*, 7105–7119. https://doi.org/10.1029/2018jb016538
Becken, M., Ritter, O., Bedrosian, P. A., & Weckmann, U. (2011). Correlation between deep fluids, tremor and creep along the central San Andreas fault. *Nature*, *480*, 87–90. https://doi.org/10.1038/nature10609
Behr, W. M., & Platt, J. P. (2014). Brittle faults are weak, yet the ductile middle crust is strong: Implications for lithospheric mechanics. *Geophysical Research Letters*, *41*, 8067–8075. https://doi.org/10.1002/2014gl061349
Boness, N. L., & Zoback, M. D. (2006). Mapping stress and structurally controlled crustal shear velocity anistropy in California. *Geology*, *34*(10), 825–828. https://doi.org/10.1130/g22309.1
Bostock, M. G. (2003). Linearized inverse scattering of teleseismicwaves for anisotropic crust and mantle structure: 1. Theory. *Journal of Geophysical Research*, *108*, 2258. https://doi.org/10.1029/2002jb001950
Bouteiller, P. L., Benjemaa, M., Metivier, L., & Virieux, J. (2019). A discontinuous Galerkin fast-sweeping eikonal solver for fast and accurate traveltime computation in 3D tilted anisotropic media. *Geophysics*, *84*(2). 1MA–Z11. https://doi.org/10.1190/geo2018-0555.1
Eaton, D. W. S. (1993). Finite difference traveltime calculation for anisotropic media. *Geophysical Journal International*, *114*, 273–280. https://doi.org/10.1111/j.1365-246x.1993.tb03915.x
Eberhart-Phillips, D., & Henderson, C. M. (2004). Including anisotropy in 3-D velocity inversion and application to Marlborough, New Zealand. *Geophysical Journal International*, *156*, 237–254. https://doi.org/10.1111/j.1365-246x.2003.02044.x
Eberhart-Phillips, D., & Michael, A. J. (1993). Three-dimensional velocity structure, seismicity, and fault structure in the Parkfield region, central California. *Journal of Geophysical Research*, *98*(B9), 15737–15758. https://doi.org/10.1029/93jb01029
Fichtner, A., & Villasenor, A. (2015). Crustal and upper mantle of the western Mediterranean—Constraints from full-waveform inversion. *Earth and Planetary Science Letters*, *428*, 52–62. https://doi.org/10.1016/j.epsl.2015.07.038
Fletcher, R., & Reeves, C. (1964). Function minimization by conjugate gradients. *The Computer Journal*, *7*, 149–154. https://doi.org/10.1093/comjnl/7.2.149

Fouch, M., & Rondenay, S. (2006). Seismic anisotropy beneath stable continental interiors. *Physics of the Earth and Planetary Interiors*, *158*, 292–320. https://doi.org/10.1016/j.pepi.2006.03.024

Gou, T., Zhao, D., Huang, Z., & Wang, L. (2018). Anisotropic 3-D ray tracing and its application to Japan subduction ZNE. *Journal of Geophysical Research: Solid Earth*, *123*, 4088–4108. https://doi.org/10.1029/2017jb015321

Hauksson, E., Yang, W., & Shearer, P. M. (2012). Waveform relocated earthquake catalog for Southern California (1981 to 2011). *Bulletin of the Seismological Society of America*, *102*(5), 2239–2244. https://doi.org/10.1785/0120120010

Hearn, T. M. (1996). Anisotropic Pn tomography in the western United States. *Journal of Geophysical Research*, *101*, 8403–8414. https://doi.org/10.1029/96jb00114

Heidbach, O., Rajabi, M., Reiter, K., Ziegler, M., & Team, W. (2016). *World Stress Map Database Release 2016* (Vol. 1.1). GFZ Data Services.

Hole, J. A., Catchings, R. D., Clair, K. C. St., Rymer, M. J., Okaya, D. A., & Carney, B. J. (2001). Steep-dip seismic imaging of the shallow San Andreas Fault near Parkfield. *Science*, *294*, 1513–1515. https://doi.org/10.1126/science.1065100

Huang, Q., Schmerr, N., Waszek, L., & Beghein, C. (2019). Constraints on seismic anisotropy in the mantle transition zone from long-period SS precursors. *Journal of Geophysical Research: Solid Earth*, *124*, 6779–6800. https://doi.org/10.1029/2019jb017307

Huang, Z., Zhao, D., & Liu, X. (2015). On the trade-off between seismic anisotropy and heterogeneity: Numerical simulations and application to Northeast Japan. *Journal of Geophysical Research: Solid Earth*, *120*, 3255–3277. https://doi.org/10.1002/2014jb011784

Jennings, C. W., & Bryant, W. A. (2010). *Fault activity map of California: California Geological Survery Geologic Data Map 2*.

Kawazoe, T., Ohuchi, T., Nishihara, Y., Nishiyama, N., Fujino, K., & Irifune, T. (2013). Seismic anisotropy in the mantle transition zone induced by shear deformation of wadsleyite. *Physics of the Earth and Planetary Interiors*, *216*, 91–98. https://doi.org/10.1016/j.pepi.2012.12.005

Kong, F., Gao, S. S., Liu, K. L., Song, J., Ding, W., Fang, Y., et al. (2018). Receiver function investigations of seismic anisotropy layering beneath southern California. *Journal of Geophysical Research: Solid Earth*, *123*, 16672–16683. https://doi.org/10.1029/2018jb015830

Laske, G., Masters, G., Ma, Z., & Pasyanos, M. (2013). Update on CRUST1.0—A 1-degree global model of Earth's crust. *Geophysical Research Abstracts*, *15*.

Leung, S., & Qian, J. (2006). An adjoint state method for three-dimensional transmission traveltime tomography using first-arrivals. *Communications in Mathematical Sciences*, *4*, 249–266. https://doi.org/10.4310/cms.2006.v4.n1.a10

Li, Z., & Peng, Z. (2017). Stress- and structure-induced anisotropy in southern California from two decades of shear wave splitting measurements. *Geophysical Research Letters*, *44*, 9607–9614. https://doi.org/10.1002/2017gl075163

Lippoldt, R., Porritt, R. W., & Sammis, C. G. (2017). Relating seismicity to the velocity structure of the San Andreas Fault near Parkfield, CA. *Geophysical Journal International*, *209*(3), 1740–1745. https://doi.org/10.1093/gji/ggx131

Liu, Y., & Tong, P. (2021). Eikonal equation-based P-wave seismic azimuthal anisotropy tomography of the crustal structure beneath northern California. *Geophysical Journal International*, *226*, 287–301. https://doi.org/10.1093/gji/ggab103

Long, M. D. (2013). Constraints on subduction geodynamics from seismic anisotropy. *Reviews of Geophysics*, *51*, 76–112. https://doi.org/10.1002/rog.20008

Long, M. D., & Becker, T. W. (2010). Mantle dynamics and seismic anisotropy. *Earth and Planetary Science Letters*, *297*, 341–354. https://doi.org/10.1016/j.epsl.2010.06.036

Long, M. D., & Silver, P. G. (2008). The subduction zone flow field from seismic anisotropy: A global view. *Science*, *319*, 315–318. https://doi.org/10.1126/science.1150809

Luo, S., & Qian, J. (2012). Fast sweeping methods for factored anisotropic eikonal equations: Multiplicative and additive factors. *Journal of Scientific Computing*, *52*, 360–382. https://doi.org/10.1007/s10915-011-9550-y

NCEDC. (2014). *Northern California Earthquake Data Center*[Dataset]: UC Berkeley Seismological Laboratory. https://doi.org/10.7932/NCEDC

Ozacar, A. A., & Zandt, G. (2009). Crustal structure and seismic anisotropy near the San Andreas Fault at Parkfield, California. *Geophysical Journal International*, *178*, 1098–1104. https://doi.org/10.1111/j.1365-246x.2009.04198.x

Piana Agostinetti, N., Giacomuzzi, G., & Chiarabba, C. (2020). Across-fault velocity gradients and slip behavior of the San Andreas Fault near Parkfield. *Geophysical Research Letters*, *47*, e2019GL084480. https://doi.org/10.1029/2019gl084480

Porter, R., Zandt, G., & McQuarrie, N. (2011). Pervasive lower-crustal seismic anisotropy in Southern California: Evidence for underplated schists and active tectonics. *Lithosphere*, *3*, 201–220. https://doi.org/10.1130/l126.1

Qian, J., Zhang, Y., & Zhao, H. (2007). A fast sweeping method for static convex Hamilton-Jacobi equations. *Journal of Scientific Computing*, *31*, 237–271. https://doi.org/10.1007/s10915-006-9124-6

Rawlinson, N., Hauser, J., & Sambridge, M. (2008). Seismic ray tracing and wavefront tracking in laterally heterogeneous media. *Advances in Geophysics*, *49*, 203–273. https://doi.org/10.1016/s0065-2687(07)49003-3

Savage, M. K. (1999). Seismic anisotropy and mantle deformation: What have we learned from shear wave splitting? *Reviews of Geophysics*, *37*, 65–106. https://doi.org/10.1029/98rg02075

SCEDC. (2013). *Southern California Earthquake Center*[Dataset]. Caltech. https://doi.org/10.7909/C3WD3xH1

Shelly, D., Ellsworth, W., Ryberg, T., Haberland, C., Fuis, G., Murphy, J., et al. (2009). Precise location of San Andreas fault tremors near Cholame, California using seismometer clusters: Slip on the deep extension of the fault? *Geophysical Research Letters*, *36*, L01303. https://doi.org/10.1029/2008gl036367

Silver, P. G., & Chan, W. W. (1991). Shear wave splitting and subcontinental mantle deformation. *Journal of Geophysical Research*, *96*, 16429–16454. https://doi.org/10.1029/91jb00899

Tape, C., Liu, Q., & Tromp, J. (2007). Finite-frequency tomography using adjoint methods-Methodology and examples using membrane surface waves. *Geophysical Journal International*, *168*, 1105–1129. https://doi.org/10.1111/j.1365-246x.2006.03191.x

Thurber, C., Zhang, H., Brocher, T., & Langenheim, V. (2009). Regional three-dimensional seismic velocity model of the crust and uppermost mantle of northern California. *Journal of Geophysical Research*, *114*, B01304. https://doi.org/10.1029/2008jb005766

Thurber, C., Zhang, H., Waldhauser, F., Hardebeck, J., Michael, A., & Eberhart-Phillips, D. (2006). Three-dimensional compressional wavespeed model, earthquake relocations, and focal mechanisms for the Parkfield, California, region. *Bulletin of the Seismological Society of America*, *96*(4B), S38–S49. https://doi.org/10.1785/0120050825

Tong, P. (2021). Adjoint-state traveltime tomography: Eikonal equation-based methods and application to the Anza area in southern California. *Journal of Geophysical Research: Solid Earth*, *126*, e2021JB021818. https://doi.org/10.1029/2021jb021818

Tong, P., Yang, D., & Huang, X. (2019). Multiple-grid model parametrization for seismic tomography with application to the San Jacinto fault zone. *Geophysical Journal International*, *218*, 200–223. https://doi.org/10.1093/gji/ggz151

Tong, P., Yao, J., Liu, Q., Li, T., Wang, K., Liu, S., et al. (2021). Crustal rotation and fluids: Factors for the 2019 Ridgecrest earthquake sequence? *Geophysical Research Letters*, *48*, e2020GL090853. https://doi.org/10.1029/2020gl090853

Townend, J., & Zoback, M. D. (2004). Regional tectonics stress near the San Andreas Fault in central and southern California. *Geophysical Research Letters*, *31*, L15S11. https://doi.org/10.1029/2003gl018918

Tromp, J., Tape, C., & Liu, Q. (2005). Seismic tomography, adjoint methods, time reversal and banana-doughnut kernels. *Geophysical Journal International*, *160*, 195–216.

Virieux, J., & Operto, S. (2009). An overview of full-waveform inversion in exploration geophysics. *Geophysics*, *74*, WCC1–WCC26. https://doi.org/10.1190/1.3238367

Waldhauser, F., & Schaff, D. P. (2008). Large-scale relocation of two decades of Northern California seismicity using cross-correlation and double-difference methods. *Journal of Geophysical Research*, *113*, B08311. https://doi.org/10.1029/2007jb005479

Wang, J., & Zhao, D. (2008). P-wave anisotropic tomography beneath Northeast Japan. *Physics of the Earth and Planetary Interiors*, *170*, 115–133. https://doi.org/10.1016/j.pepi.2008.07.042

Wang, K., Jiang, C., Yang, Y., Schulte-Pelkum, V., & Liu, Q. (2020). Crustal deformation in southern California constrained by radial anisotropy from ambient noise adjoint tomography. *Geophysical Research Letters*, *47*, e2020GL088580. https://doi.org/10.1029/2020gl088580

Wang, Y. (2014). Seismic ray tracing in anisotropic media: A modified Newton algorithm for solving highly nonlinear systems. *Geophysics*, *79*, T1–T7. https://doi.org/10.1190/geo2013-0110.1

Wang, Z., Fukao, Y., Kodaira, S., & Huang, R. (2008). Role of fluids in the initiation of the 2008 Iwate earthquake (M7.2) in northeast japan. *Geophysical Research Letters*, *35*, L24303. https://doi.org/10.1029/2008gl035869

Wessel, P., & Smith, W. H. F. (1991). Free software helps map and display data. *Eos, Transactions American Geophysical Union*, *72*(1), 441–448. https://doi.org/10.1029/90eo00319

Yang, Z., Sheehan, A., & Shearer, P. (2011). Stress-induced upper crustal anisotropy in southern California. *Journal of Geophysical Research*, *116*, B02302. https://doi.org/10.1029/2010jb007655

Zeng, X., Thurber, C. H., Shelly, D. R., Harrington, R. M., Cochran, E. S., Bennington, N. L., et al. (2016). 3-D P- and S-wave velocity structure and low-frequency earthquake locations in the Parkfield, California region. *Geophysical Journal International*, *206*(3), 1574–1585. https://doi.org/10.1093/gji/ggw217

Zhao, D., Yu, S., & Liu, X. (2016). Seismic anisotropy tomography: New insight into subduction dynamics. *Gondwana Research*, *33*, 24–43. https://doi.org/10.1016/j.gr.2015.05.008

Zhu, H., Bozdag, E., & Tromp, J. (2015). Seismic structure of the European upper mantle based on adjoint tomography. *Geophysical Journal International*, *201*(1), 18–52. https://doi.org/10.1093/gji/ggu492